Sexual dimorphism in sensorimotor transformation of optic flow

Sarah Nicholas[1], Katja Sporar Klinge[1#], Luke Turnbull[1], Annabel Moran[1], Aika Young[1], Yuri Ogawa[1], Karin Nordström[1,2*]*

[1]Flinders Health and Medical Research Institute, Flinders University, GPO Box 2100, Adelaide, SA, 5001, Australia; [2]Department of Medical Cell Biology, Uppsala University, 75123 Uppsala, Sweden.

[#]Current address: Institute for Developmental Biology, RWTH Aachen University, 52074 Aachen, Germany

*Shared authorship; email: yuri.ogawa@flinders.edu.au; karin.nordstrom@flinders.edu.au

ORCIDs

Sarah Nicholas: 0000-0002-5555-9421

Katja Sporar Klinge: 0009-0004-7224-6568

Aika Young: 0009-0000-5028-6164

Yuri Ogawa: 0000-0002-9708-7063

Karin Nordström: 0000-0002-6020-6348

CRediT author statement

Sarah Nicholas: conceptualization, methodology, validation, formal analysis, investigation, data curation, writing – original draft, visualization, project administration; **Katja Sporar**

Klinge: methodology, validation, formal analysis, investigation, data curation, writing – review and editing, visualization; **Luke Turnbull:** methodology, validation, investigation, writing – review and editing; **Annabel Moran:** investigation, writing – review and editing; **Aika Young**: investigation, writing – review and editing; **Yuri Ogawa:** methodology, validation, formal analysis, investigation, data curation, writing – original draft, visualization, supervision, project administration; **Karin Nordström:** conceptualization, validation, formal analysis, resources, writing – original draft, visualization, supervision, project administration, funding acquisition.

Abstract

Motion vision underpins a wide range of adaptive behaviours essential for individual and species survival. In hoverflies, some visual behaviours are sexually dimorphic, including for example male high-speed pursuit of conspecifics, matched by improved optics, and faster photoreceptors. Other visual behaviours are sexually monomorphic, with for example similar foraging flight speeds in male and female hoverflies. However, whether the descending neurons responsible for sensorimotor transformation of optic flow are sexually dimorphic is unknown. To address this, we combined morphological analysis with electrophysiology of optic flow sensitive descending neurons and compared neural responses to the behavioural output in tethered hoverflies. We found that while optomotor flight behaviour is largely sexually monomorphic, the underlying neural responses are sexually dimorphic, especially at higher optic flow velocities. Additionally, behavioural responses were noticeably slower than neural responses. Together, our findings uncover a nuanced, sex- and stimulus- dependant sensorimotor transformation, shaped by both neural architecture and behavioural demands.

Keywords

Sexual dimorphism, hoverfly, descending neuron, optic flow, optomotor response

Introduction

Motion vision is a fundamental sensory modality across the animal kingdom, enabling animals to navigate, to maintain a straight trajectory, to avoid collisions, and to identify prey, predators or mates. Among the most potent cues for self-motion is widefield optic flow, the coherent motion of the entire visual field, generated by an animal's own movement through the world. In insects, the neural mechanisms underlying optic flow processing have been studied extensively (for a review, see e.g. Ref [1]), offering a powerful model for understanding how compact nervous systems extract behaviourally relevant information from dynamic visual scenes.

To generate appropriate responses to widefield optic flow, the visual input needs to be integrated across space. In flies, this spatial pooling occurs in 45-60 lobula plate tangential cells (LPTCs)[2,3], each matched to a particular type of self-generated optic flow[4], where the horizontal system (HS) and vertical system (VS) cells are the most well described. HS cells respond optimally to rotations around the yaw axis, whereas VS cells are tuned to pitch and roll rotations[5]. LPTCs project to the inferior posterior slope[6], where they synapse with descending neurons[7,8]. In *Drosophila* at least 35 descending neuron types have their inputs in the posterior surface of the brain (named DNp1-35)[9]. Furthermore, in *Drosophila* and blowflies, three of these descending neurons have been shown to respond robustly to widefield optic flow. Their axons project to the dorsal part of the thoracic ganglion, where motor neurons controlling the neck, wings and halteres are located[7,10-13].

64 DNp15, also called DNHS1, receives input from HS cells[9-11] and is physiologically similar to
65 the optic flow sensitive descending neuron type 1 (OFS DN1) in the hoverfly *Eristalis*
66 *tenax*[14], although direct LPTC coupling has not yet been demonstrated in the hoverfly.
67 DNHS1 projects to the neck and haltere motor neuropils[9] and has been implicated in the
68 control of head yaw movements, abdominal ruddering and flight stabilization via the haltere
69 motor system[10]. DNp20, or DNOVS1, receiving input from the ocelli and VS cells[7,9,10,15], is
70 likely involved in rapid head movements[9], possibly facilitating gaze stabilization during
71 flight[10]. DNp22, or DNOVS2, also receives input from the ocelli but a different subset of VS
72 cells[7,9,10,16]. DNOVS2 is physiologically similar to the *Eristalis tenax* optic flow sensitive
73 descending neuron type 2 (OFS DN2)[14], but synaptic coupling with VS cells has not been
74 shown in hoverflies. DNOVS2 projects to the neck, wing and haltere motor neuropils[9] and
75 has been implied in the initiation of the fast body saccades that support rapid re-orientation[10]
76 during flight in response to dynamic visual cues.

77 Hoverflies are interesting in the context of motion vision, which they use both to maintain a
78 hovering stance, and to fly at high speed[17]. Indeed, hoverflies show striking sexually
79 dimorphic flight behaviour, where males establish territories which they guard rigorously
80 from a hovering stance[18], followed by high-speed flight to chase away any intruding insects
81 and/or pursue conspecific females for courtship and mating[17,19]. Male hoverflies are also
82 smaller than females[20,21], which introduces an aerodynamic component by reducing inertia
83 and enabling finer control over rapid flight adjustments[22]. Accompanying this sexually
84 dimorphic pursuit behaviour, male *E. tenax* have larger lenses than females in a dorso-frontal
85 bright zone[23], with faster motion detection and increased signal-to-noise ratio[24]. In many fly

species, the photoreceptors in this part of the eye are also faster in males[25]. In hoverflies, even if the LPTCs are typically implied in optomotor responses[1], males have a smaller HSN receptive field[26] and velocity tuning shifted to higher velocities[23,27]. These adaptations are likely useful in regulating optomotor responses during high-speed target pursuit[28,29]. Indeed, as target selective descending neurons (TSDNs) are suppressed when target and background move in the same direction[28,30], the optic flow sensitive descending neurons may serve a complementary role in stabilizing flight under these conditions.

The differences in optics, photoreceptor dynamics, and LPTC receptive field size and velocity tuning, have been interpreted as required by males in the fast flight used during sexually dimorphic territorial behaviours. Interestingly, there is no sexual dimorphism in flight speed during behaviours likely to be governed primarily by the LPTCs, such as foraging between flowers[31] and when flying within the confines of an indoor arena[32]. To investigate the discrepancy between sexually dimorphic visual processing and sexually monomorphic flight speed, we compared the electrophysiological response characteristics and morphology of optic flow sensitive descending neurons in male and female hoverflies and linked these findings to the behaviour of tethered hoverflies viewing similar stimuli. We used the wing beat amplitude (WBA) as a measure of the optomotor response, and found no sexual dimorphism at speeds up to 2 m/s for translation and 200°/s for rotation. While the head movements were largely sexually monomorphic, the extension of the fore- and hind legs exhibited clearer sexual dimorphism. Furthermore, while neural morphology, receptive fields and direction sensitivity of the descending neurons showed minimal sex differences, there was a significant and noticeable difference in the velocity response functions between males

108 and females, especially at higher speeds. Critically, neural differences were not only velocity
109 dependent but also varied between stimuli (occurring only for sideslip, lift and thrust, but not
110 roll) and neuron type. These neuron-, stimulus-, and sex-specific differences uncovers a
111 previously unrecognized complexity in the neural encoding of visual motion, revealing for
112 the first time, a sex-dependent transformation from sensory input to motor output.

113 Results

114 Two distinct types of optic flow sensitive descending neurons can be identified by their
115 receptive field location and preferred direction

116 Optic flow sensitive descending neurons can be readily identified by mapping their receptive
117 field using small sinusoidal gratings[14,23]. Based on the receptive fields of 100 reference
118 neurons recorded from 90 male hoverflies, we found that two key parameters, the azimuthal
119 position of the receptive field centre and its preferred direction of motion, are sufficient to
120 reliably ascertain neuron type (Fig. 1, Supplementary Fig. 1). OFS DN1 has a preferred
121 direction up and away from the midline, either leftward (range from 137° to 171°) or
122 rightward (range from 16° to 40°) for neurons on the left- and right-hand side of the visual
123 field, respectively (Fig. 1a, b and c; green, Fig. 1g, h and i). OFS DN2 neurons respond
124 preferentially to downward motion (range from 228° to 293°; Fig. 1d, e and f; yellow and
125 orange, Fig. 1g, h and i) with the azimuthal position of the receptive field centre separating
126 left-hand side (LHS) from right-hand side neurons (RHS, Fig. 1g, h and i).

127 We used the maximum local motion sensitivity (LMS, Fig. 1c, f), the extent of the receptive
128 fields (number of positions with LMS over 50%, arrows in Fig. 1c, f) and the local preferred
129 direction (LPD, Fig. 1c, f) variance from these 100 reference neurons (grey data,
130 Supplementary Fig. 2a, b and c) to set strict exclusion criteria (dashed red, Supplementary
131 Fig. 2a, b and c) of the neurons used in the rest of the paper. This resulted in the exclusion of
132 two neurons from males and seven from females (grey, Supplementary Fig. 2d, e) due to
133 either low LMS (less than 20 spikes/s, Supplementary Fig. 2a), a small number of locations
134 where LMS exceeded 50% of the maximum (four positions or less, Supplementary Fig. 2b)
135 or high LPD variance (above 30°, Supplementary Fig. 2c).

136 We found no sexual dimorphism in either neuron type when comparing receptive field width
137 and height of the remaining 33 male and 29 female neurons (Supplementary Fig. 2f, unpaired
138 t-test, $p = 0.52$ and 0.09 for width and height of OFS DN1, and $p = 0.19$ and 0.13 for width
139 and height of OFS DN2).

140 **Directional tuning of optic flow sensitive descending neurons exhibits limited sexual**
141 **dimorphism**

142 Some LPTCs, which are upstream of optic flow sensitive descending neurons, show distinct
143 sexual dimorphism, whilst others do not[23,26]. The receptive field data used for classifying
144 OFS DN1 and DN2 showed that they are strongly directional (Fig. 1g, i). To investigate if
145 this direction tuning is sexually dimorphic, we used a separate experiment quantifying
146 responses to full-screen sinusoidal grating stimuli (wavelength 7°, 5 Hz, Supplementary Fig.
147 3). We found that the resulting preferred direction of both OFS DN1 and OFS DN2 matched

148 their receptive field preferred directions (compare polar plots in Supplementary Fig. 2d, e
149 with Supplementary Fig. 3g, h), i.e. up and away from the visual midline for OFS DN1
150 (range from 359° to 52°) or downwards for OFS DN2 (range from 273° to 297°, Fig. 2a).
151 Whilst OFS DN1 showed no difference in preferred direction between the sexes (Watson-
152 Williams two-sample test, $p = 0.38$), male OFS DN2 had a slightly more lateral preferred
153 direction compared to females (Fig. 2a; median = 285.4° compared to 281.5°, Watson-
154 Williams two-sample test, $p = 0.046$).

155 We quantified the spontaneous rate and found that neither this nor the responses of OFS DN1
156 to a stationary starfield pattern differed between the sexes (circles, Supplementary Fig. 4a,
157 two-way ANOVA, $p = 0.29$). Conversely, OFS DN2 exhibited significant sexual
158 dimorphism, with females displaying a higher spontaneous rate and response to stationary
159 stimuli than males (circles, Supplementary Fig. 4b, two-way ANOVA, $p < 0.001$). The
160 response to a stationary stimulus was larger than spontaneous rate in males ($p = 0.015$), but
161 not in females (red circles, Supplementary Fig. 4b, $p = 0.35$, two-way ANOVA).

162 We next looked at the responses to moving full-screen 3-dimensional starfield stimuli
163 simulating the type of optic flow that would be generated by self-motion through space[33] (at
164 0.5 m/s for translations and 50°/s for rotations), after subtracting the response to the
165 stationary stimulus (filled circles, Supplementary Fig. 4a, b). As predicted from the receptive
166 fields (Fig. 1) OFS DN1 was excited by stimuli moving either up or away from the midline,
167 such as rightward sideslip and yaw, and upwards lift and pitch (Fig. 2b), whilst OFS DN2
168 showed the strongest responses to downwards lift and pitch (Fig. 2c). Both neuron types

169 respond strongly to clockwise roll (Fig. 2b, c), as predicted by their receptive fields (Fig. 1a,
170 b) and shown previously for males[14]. However, neither neuron type showed any sexual
171 dimorphism (Fig. 2b, c, two-way ANOVA, $p = 0.81$ and 0.92, OFS DN1 and OFS DN2,
172 respectively).

173 **Sexual dimorphism in optic flow descending neurons is velocity dependent**

174 As the velocity tuning of some LPTCs is sexually dimorphic[23,27], we tested the responses of
175 optic flow sensitive descending neurons using a continuous velocity step stimulus (Fig. 3,
176 Supplementary movie 1). Six velocities for each direction of the stimuli (e.g. anticlockwise
177 roll -10 to -200°/s and clockwise roll +10 to +200°/s) and a stationary control were presented
178 three times each in random order for 2 s each (see example, Fig. 3a).

179 We confirmed that the spontaneous rate and response to stationary stimuli was significantly
180 higher in females compared to males for OFS DN2 but not for OFS DN1 (triangles,
181 Supplementary Fig. 4a, b, two-way ANOVA, $p = 0.18$ and $p < 0.001$, OFS DN1 and OFS
182 DN2, respectively). As above, we subtracted the average response to the stationary stimulus
183 from the responses to moving optic flow. The resulting data show that both neuron types
184 exhibit sexual dimorphism to certain types of optic flow (Fig. 3e, f and Table 1). For
185 example, the OFS DN1 response to thrust show a significant interaction between sex and
186 velocity, with female neurons responding stronger to positive thrust compared to males (Fig.
187 3e and Table 1). The OFS DN2 response to sideslip was significantly different between males
188 and females, and there was a significant interaction between sex and velocity in the responses

189 to sideslip, lift, and thrust, with males responding stronger to sideslip, lift and thrust (Fig. 3f
190 and Table 1).

191 **Morphological reconstruction suggests optic flow sensitive descending neurons could**
192 **control the wings**

193 By recording from the descending neurons intracellularly we could iontophoretically fill them
194 with 3% neurobiotin following identification based on receptive field (as in Fig. 1). We found
195 that OFS DN1 and OFS DN2 of either sex receive their input in the part of the brain where
196 LPTCs have their output (Fig. 4a, b, d, e and f). Both neuron types project along the length of
197 the thoracic ganglion, with several fine branches along the way (Fig. 4a, b, c, g, h and i), like
198 *Drosophila* DNHS1 and DNOVS2[34]. In *Drosophila*, DNOVS2 projects more medially than
199 DNHS1, which also has a more distal projection, close to the haltere nerve (HN)[34]. However,
200 we saw no such differences between the projections of OFS DN1 and DN2 (Fig. 4a, b, c, g, h
201 and i). In addition, both hoverfly neuron types have prominent outputs where the prothoracic
202 and pterothoracic nerves likely get their inputs (T1 LN and PtN, Fig. 4a, b, c, g, h and i),
203 which is more similar to the outputs of *Drosophila* DNOVS1[34]. These outputs suggest that
204 OFS DN1 and DN2 could contribute to controlling the neck, wings and/or the forelegs.

205 Whilst there was no indication of extensive sexual dimorphism in the structural morphology
206 of these neurons, OFS DN2 appears to be slightly wider along the length of the cervical
207 connective in females (Supplementary Fig. 5a, b). In part, this may be due to female
208 hoverflies being bigger[20,21] and therefore having a wider cervical connective (Supplementary
209 Fig. 5c).

210 **Wing beat amplitude changes are velocity dependent but not sexually dimorphic**

211 Given that the morphological data suggest that both neuron types could control the wings
212 (Fig. 4), we conducted behavioural experiments in an open-loop tethered flight arena using
213 the same continuous velocity stimulus as in electrophysiology (see Fig. 3a). We tracked the
214 wing beat amplitude (WBA) for each wing (Fig. 5a, b, Supplementary movie 2) using
215 DeepLabCut models[35,36] while the tethered animal was viewing different starfield velocities
216 (Fig. 5c, d, e and f). Changes in the sum of the left and right WBA (WBAS, Fig. 5b) reflect
217 variations in flight force generation, potentially contributing to either lift or thrust, while the
218 difference between left and right WBA (WBAD) indicates yaw turning behaviour[37-39] or
219 adjustments to body orientation[40].

220 The male WBAS is higher when viewing stationary stimuli compared with pre-stimulation
221 ("pre stim" in Fig. 5c, d; blue, Supplementary Fig. 4c, two-way ANOVA followed by
222 Uncorrected Fisher's LSD test, $p < 0.01$). However, there was no sexual dimorphism in the
223 WBAS during pre-stimulation, nor when viewing stationary stimuli (Supplementary Fig. 4c,
224 two-way ANOVA, $p = 0.35$). When comparing responses to each type of optic flow, after
225 subtracting the response to stationary stimuli, both the WBAD and WBAS depended strongly
226 on velocity, however, there was no sexual dimorphism (Fig. 5g, h and Table 2).

227 The lack of sexual dimorphism observed in behaviour (Fig. 5g, h and Table 2) contrasts with
228 the neural responses (Fig. 3e, f and Table 1). Additionally, it is difficult to align the WBA
229 responses to different types of optic flow with the neuronal input. For example, in response to
230 higher clockwise roll velocities of (100 - 200°/s), hoverflies exhibit a decreased WBAD

231 (positive roll, Fig. 5g) and a slightly increased WBAS (positive roll, Fig. 5h) indicating either
232 a leftward turn or an anticlockwise body correction. Similarly, both RHS neuron types give
233 strong responses to clockwise roll (positive roll, Fig. 3e, f). However, sideslip moving
234 leftwards also elicits a decreased WBAD (negative sideslip, Fig. 5g) and an increased WBAS
235 (negative sideslip, Fig. 5h) but neither neuron type responds strongly to this (negative
236 sideslip, Fig. 3e, f).

237 We found that neither lift nor thrust evoke large turning responses (Fig. 5g), however, large
238 and significant increases in the WBAS were observed in hoverflies experiencing the
239 sensation of falling (positive lift, Fig. 5h and Table 2) or being pushed backwards (negative
240 thrust, Fig. 5h and Table 2). Interestingly, each neuron type responds to lift and thrust in a
241 different manner, with OFS DN1 being excited by upwards lift and approaching thrust (Fig.
242 3e), whereas OFS DN2 is excited by downwards lift and receding thrust (Fig. 3f).

243 In electrophysiology we used a horizontally oriented visual monitor (Supplementary Fig. 6a),
244 whereas in behaviour the monitor was rotated 90° (Supplementary Fig. 6b and Ref [36]). To
245 ensure that this did not substantially affect the shape of the velocity-response functions, we
246 reduced the stimuli to the central square in both behaviour and electrophysiology. This
247 reduction caused a slight but significant change in neuronal (central square; Supplementary
248 Fig. 6c, two-way ANOVA, $p = 0.04$) and WBAS responses (central square; Supplementary
249 Fig. 6d, two-way ANOVA, $p = 0.04$). However, it did not alter the shape of the velocity
250 response function nor produce a significant interaction between velocity and screen size
251 (two-way ANOVA, $p = 0.36$ and 0.49, OFS DN2 and WBAS, respectively).

252 **Response onset depends on stimulus type**

253 It has been previously shown that while neuronal responses are fast[33] behavioural responses
254 occur on a much slower time scale and differ depending on stimulus type[41,42]. We here found
255 that there is no significant effect of sex on either neuronal or WBAS response onset (Fig. 6,
256 two-way ANOVA, $p = 0.21$, 0.79 and 0.31, OFS DN1, OFS DN2 and WBAS, respectively).
257 However, the onset for roll compared to lift is significantly longer for OFS DN2 and WBAS
258 but not for OFS DN1 (Fig. 6, two-way ANOVA, $p < 0.0001$ for both OFS DN2 and WBAS
259 compared to $p = 0.08$ for OFS DN1). Note that we recorded the WBA from above (Fig. 5a),
260 and as such did not quantify wing rotations and adjustments outside of the horizontal plane.
261 The WBA response onset to roll optic flow (Fig. 6c) should thus be viewed as highly
262 conservative.

263 **Sideslip and lift optic flow generate strong head, fore- and hind leg movements**

264 The lack of sexual dimorphism in WBA suggests that behavioural responses to optic flow are
265 the same between the sexes. To investigate this further, we next extracted the head angle
266 (Fig. 7a, b), and the extension of the fore- (Fig. 7a, c) and hind legs (Fig. 7a, d). We found
267 that the head turned significantly when viewing sideslip (Supplementary movie 2 and 3, Fig.
268 7e and Table 2, two-way ANOVA, $p < 0.001$ for velocity), but there was no response to the
269 other three types of optic flow. We found no sexual dimorphism (Fig. 7e and Table 2).

270 We found that while the forelegs could not be seen in the dorsal view for most of the flight
271 (see e.g. Fig. 5a), they extended anteriorly in response to high velocity sideslip, lift and

272 thrust, but not to roll (Fig. 7f , Table 2 and Supplementary movie 2-9). The foreleg extension
273 to sideslip was sexually dimorphic, with significant interaction between sex and velocity for
274 sideslip and lift motions (Fig. 7f and Table 2, two-way ANOVA, $p = 0.04$, 0.01, 0.03,
275 respectively). Post hoc pairwise comparisons revealed females extended their forelegs further
276 than males to upwards lift at 1.5 m/s (Fig. 7f, Šídák's multiple comparisons test, $p = 0.01$).

277 The hind legs were generally extended during flight (Fig. 5a, Fig. 7a) with males extending
278 their legs further than females (Supplementary Fig. 4d, two-way ANOVA, $p = 0.032$). After
279 subtracting the hind leg extension when viewing the stationary starfield (filled symbols,
280 Supplementary Fig. 4d), we found similar patterns to foreleg extension (Fig. 7f), with a
281 significant interaction between sex and velocity only in response to sideslip (Fig. 7g and
282 Table 2, two-way ANOVA, $p = 0.02$). We quantified the difference between the right and the
283 left hind leg and found that there was a significant interaction between sex and velocity in
284 response to roll and thrust (Fig. 7h and Table 2, two-way ANOVA, $p = 0.02$ for roll and
285 $p < 0.0001$ for thrust).

286 Looking at the different body parts together we noted that in response to upwards lift
287 (generating a falling sensation) the WBAS increases substantially (Fig. 5h), and the fore-
288 (Fig. 7f) and hind legs (Fig. 7g) all extend, potentially to brace for impact (Supplementary
289 movie 4 and 5). We also noted that in response to sideslip, the WBAS increases (Fig. 5h), the
290 WBAD indicates a turn in the direction of the optic flow (Fig. 5g), the head rotates (Fig. 7e),
291 and both the forelegs and hind legs extend (Fig. 7f, g). The hind legs appear to be ruddering,
292 with the right leg extending more when the animal is turning right (Fig. 5g, 7h,

293 Supplementary movie 2 and 3). There was no significant difference in the response onset of
294 these body parts, nor was there any sexual dimorphism (Supplementary Fig. 7).

295 Discussion

296 In the hoverfly, the optics, photoreceptors, and HS cells exhibit clear sexual
297 dimorphism[23,24,26,27]. In line with this, our findings reveal that optic flow sensitive descending
298 neurons also show sexually dimorphic velocity response functions (Fig. 3). Yet, despite the
299 multi-level anatomical and neural sexual dimorphism, the wing beat amplitude (Fig. 5) and
300 head movements (Fig. 7) remain mostly monomorphic, while leg movements exhibit clear
301 sex-specific differences. Moreover, differences between neural and behavioural velocity
302 response functions (Fig. 3, 5, 7) and response latency (Fig. 6) highlight the likely
303 involvement of downstream processing mechanisms that could reconcile sex-specific sensory
304 encoding with conserved flight control.

305 Some hoverfly flight behaviours are strongly sexually dimorphic, such as those related to
306 courtship and mating. For example, male hoverflies defend territories from a hovering stance
307 from which they pursue and capture female conspecifics at high speeds[19]. In contrast, other
308 behaviours, including cruising speeds in field[31] and indoor settings[32] do not differ between
309 sexes, and are much slower (median around 0.3 m/s[31,32]) than the 10 m/s that can be reached
310 during outdoor pursuit[19]. In comparison, our results show limited sex-related differences in
311 WBA in response to optic flow speeds up to 2 m/s (Fig. 5), yet we detected pronounced
312 sexual dimorphism in neural responses at velocities as low as 0.5 m/s (Fig. 3, Table 1). This
313 suggests that sensory processing differences emerge at lower velocities than the velocities

where motor output diverges. Moreover, the WBAS response latencies were much longer than the corresponding neural activity (Fig. 6), implying that temporal integration or additional circuit-level modulation may delay and refine motor execution. Together, these findings suggest a complex transformation between sex-specific sensory encoding and conserved motor behaviour, potentially mediated by downstream integration or additional alternate neural pathways that bypass the descending neurons studied here.

In *Drosophila* there are around 1000 descending neurons, of which at least 35 types receive their input in the posterior surface of the brain, which includes the inferior posterior slope, where the LPTC outputs are found[6,7,9]. However, only a subset of these constitute the 29 descending neuron types that project to the wing motor neuropil[9]. It is thus likely that the WBA that we recorded here (Fig. 5) reflects contributions from descending neurons beyond the two that we have characterised (Fig. 1, 3) in this study. For example, many looming sensitive neurons also respond to widefield optic flow[14,43] and could therefore play a role in the WBA changes that we detected (Fig. 5). While the morphology of both neurons (Fig. 4) suggested involvement in wing motor control, there is currently no direct evidence implicating them in the control of wingbeat amplitude. Interestingly, DNOVS2 in *Drosophila*, a physiologically similar neuron to OFS DN2[14], has been indirectly linked to rapid turning behaviour[10]. Furthermore, silencing HS and VS cells, the presumed presynaptic LPTCs to these descending neurons, results in reductions in WBA only at higher stimulus speeds[44]. These findings suggest that HS and VS cells, along with their downstream targets, may be specialized for driving fast optomotor responses under high-speed visual motion

335 (>180°/s), rather than broadly regulating WBA across all velocities, including those
336 examined in this study.

337 Beyond their potential involvement in wingbeat amplitude modulation, OFS DNs may play a
338 role in coordinating head and body positioning during flight, especially in contexts requiring
339 precise visual alignment and rapid manoeuvring. Indeed, the *Drosophila* physiological
340 homologs of OFS DN1 and OFS DN2[14], DNHS1 and DNOVS2, project to the neck motor
341 neuropil[9], and have been implicated in controlling head movements, abdominal ruddering,
342 and engagement with the haltere motor system for flight stabilization[10]. While we did not
343 quantify abdominal or haltere movements, we found that the head turned when viewing
344 sideslip optic flow (Fig. 7e), and that the velocity dependence was similar to neural (Fig. 3e)
345 and WBAD (Fig. 5g) responses. While we did not detect any head movements to roll, lift or
346 thrust, this could be a technical limitation of recording from above (Fig. 5a). Indeed, many of
347 the 29 descending neuron types that project to the wing motor neuropil, also project to the
348 neck motor neuropil[9], suggesting that synchronized responses are not unexpected. Neither are
349 the similar responses of the fore- and hind legs surprising (Fig. 7, f and g), considering that in
350 *Drosophila* many of the ~30 descending neuron types that project to the forelegs, also project
351 to the mid- and hind legs[9].

352 Our WBA recordings would also be affected by filming from above and thus lacking other
353 nuanced changes in wing angles. Thus, the sexual dimorphism in neural responses (Fig. 3)
354 could reflect an evolutionary tuning of visuomotor pathways in males, optimized for fast,
355 directional adjustments rather than gross changes in WBA in the horizontal plane. For

356 instance, whilst changes in WBAS are similar when generating either lift or thrust (Fig. 5h),
357 body pitch dynamically adjusts their ratio, driving behavioural variation[45]. Thus, OFS DNs
358 may serve as integral components of a broader flight control architecture, interfacing optic
359 flow detection with dynamic body and head positioning systems to support complex, sex-
360 specific behavioural outcomes, particularly in males engaging in high-speed pursuits.

361 Indeed, flight speed in insects results from a complex integration of multiple kinematic
362 parameters, not solely from changes in wingbeat amplitude. Many species refine their
363 aerodynamic output by modulating wingbeat frequency, angle of attack, wing tip trajectory,
364 deviations from the mean stroke plane and through precise adjustments to the timing and
365 duration of the up- and downstrokes[46]. These control strategies support agile manoeuvring,
366 particularly during visually guided behaviours such as the high-speed pursuits undertaken by
367 male hoverflies. Furthermore, the smaller body size of male hoverflies compared to
368 females[20,21] may confer biomechanical advantages, including reduced mass, facilitating faster
369 acceleration, heightened responsiveness, and lower metabolic costs for executing flight
370 manoeuvres[22,47], which do not appear in a tethered flight set-up. Such enhanced agility is
371 likely crucial for rapid direction changes required during courtship and may enable male
372 hoverflies to outperform female flies without relying on increased wingbeat amplitude.

373 Taken together, our findings reveal significant differences between sexually dimorphic
374 sensory encoding and conserved motor output in hoverfly flight at cruising speeds. Although
375 OFS DNs and their upstream visual circuits display clear sex-specific tuning, wingbeat
376 amplitude and head angle changes in response to optic flow stimuli remain relatively similar

377 between the sexes, suggesting additional mechanisms downstream of sensory input. This
378 likely reflects a complex interplay of biomechanical properties, multisensory integration and
379 circuit-level modulation, each shaping and refining behavioural outcomes to meet distinct
380 demands, preserving the consistency of low-speed manoeuvres whilst enabling sex-specific
381 tuning during high-speed pursuits.

382 # Methods

383 ## Animals

384 For all experiments, male and female *Eristalis tenax* were reared and housed as described
385 previously[21]. Briefly, eggs were collected from females captured under permit in Wittunga
386 Botanic Garden, Adelaide, South Australia. Upon hatching, larvae were reared in a rabbit
387 dung slurry until third instar larvae emerged to pupate. Eclosion occurred 1-2 weeks post-
388 pupation. Adult hoverflies were used for behavioural experiments at 17-87 days post-
389 eclosion, for intracellular electrophysiology and subsequent morphological reconstruction at
390 38-54 days, and for extracellular electrophysiology at 8-204 days.

391 ## Electrophysiology

392 Before recording the animal was immobilised, mounted dorsal side down (Supplementary
393 Fig. 6a) and secured using a mixture of beeswax and resin. A small region of cuticle was
394 removed at the anterior end of the thorax to expose the cervical connective. If required, any
395 excessive gut or tracheal tissue obstructing the recording site was removed and a small
396 volume of PBS was added to prevent drying within the ventral cavity. A fine wire hook was

397 positioned under the cervical connective for mechanical support, and a silver wire was
398 inserted into the cavity to serve as a reference electrode and grounding wire[14].

399 For extracellular recordings, a sharp tungsten microelectrode (2 MΩ, polyimide-insulated;
400 Microprobes) was inserted into the cervical connective[14]. Signals were amplified 1000 times
401 and band-pass filtered between 10–3000 Hz using a DAM50 differential amplifier (World
402 Precision Instruments), followed by noise reduction with a HumBug (Quest Scientific). Data
403 were digitized via a PowerLab 4/30 interface (ADInstruments) and acquired at 40 kHz. Spike
404 sorting was performed in LabChart 7 Pro (ADInstruments) based on the amplitude and width
405 of individual action potentials.

406 For intracellular recordings, aluminosilicate electrodes were pulled using a Sutter P-1000
407 micropipette puller, achieving a resistance of approximately 40-70 MΩ. Electrode tips were
408 filled with 3% neurobiotin (Vector Laboratories), then backfilled with 1 M KCl using a
409 syringe, leaving a small air bubble between the two solutions. Electrodes were inserted into
410 the cervical connective for recording, and the resulting signal was amplified using an
411 Axoclamp-2B amplifier (Axon Instruments), followed by 50 Hz noise reduction with a
412 HumBug (Quest Scientific). Data acquisition and digitization were performed at 10 kHz
413 using an NI USB-6210 16-bit data acquisition card (National Instruments) and the MATLAB
414 Data Acquisition Toolbox (Mathworks), using in house software
415 (https://github.com/HoverflyLab/SampSamp).

416 **Morphological reconstructions**

417 Following intracellular recordings, neurons were stained iontophoretically with neurobiotin
418 using currents in the 1 nA range for 3–12 minutes. The nervous system was then carefully
419 dissected and fixed in 4% paraformaldehyde overnight. Tissue was incubated with a Cy3-
420 streptavidin conjugate (1:100; Jackson ImmunoResearch) for 2 hours, then dehydrated
421 through an ethanol series (50–100%) for 15-20 minutes per step. After washing in PBT, the
422 tissue was cleared in RapiClear (SUNJIN Lab) and mounted with spacers. Imaging was
423 performed using a Zeiss LSM 880 Fast Airyscan confocal microscope at the institutional
424 microscopy facility. Neuron morphology and cervical connective width were quantified using
425 ImageJ[48].

426 **Tethered flight**

427 Prior to flight recordings, hoverflies were tethered at a 32° angle (Supplementary Fig. 6b)
428 using a beeswax–resin mixture to a small pin inserted into a hypodermic needle (BD
429 Microlance, 23G × 1¼"). Flight was initiated by manually providing airflow for 1–10
430 minutes until consistent flight behaviour was observed. Once positioned facing the centre of
431 the visual monitor (Supplementary Fig. 6b), hoverflies were filmed from above at 100 Hz
432 using a Sony PlayStation 3 Move Eye Camera (SLEH- 00448, Sony) with the IR filter
433 removed, and equipped with an infrared pass filter (R72 INFRARED, 49 mm, HOYA; for
434 details see Ref[36]). Illumination was provided by infrared LEDs inserted into USB lights
435 (JANSJÖ LED USB lamp, IKEA) and a Musou Black (Shin Kokushoku Musou black,

436 KOYO Orient Japan) surface was placed beneath the hoverfly to enhance contrast and
437 minimize optical interference.

438 We used DeepLabCut (DLC) version 2.3.3[35] to train a model to track the thorax, the peak
439 downstroke angle, referred to as the wing beat amplitude (WBA), of the left and right wing
440 (WBA_L and WBA_R; Fig. 5a, b), as described previously[36]. In addition, we tracked the dorso-
441 medial head (yellow, green, Fig. 7a, b), the proximal and distal points of the forelegs (blue,
442 Fig. 7a, c), the hind leg knee and the lateral, mid-abdomen (magenta, green, Fig. 7a, d). For
443 this purpose, we first manually labelled the anatomical landmarks (Fig. 5a and Fig. 7a),
444 across 16 extracted video frames per individual from four hoverflies (2 males, 2 females). In
445 addition to examples where the hoverfly was not flying, these frames included responses to
446 yaw rotation and forward translation. The DLC model was trained for 300,000 iterations,
447 yielding train and test errors of 1.2 and 1.16 pixels, respectively.

448 To identify potential tracking errors from DLC, we smoothed the WBA time series using
449 MATLAB's *smooth* function with both *loess* and *rloess* methods. Because *rloess* is more
450 resistant to outliers, we used it to detect abnormal data points. For each wing, if the absolute
451 difference between the *loess*- and *rloess*-smoothed signals exceeded 5% for more than 1 s,
452 the data were excluded due to suspected tracking artifacts. The smoothing was used only for
453 error detection; all subsequent analyses were performed on the unsmoothed data. In addition,
454 we excluded data if the WBA of either wing dropped below 40° for at least 0.5 s, as this
455 indicated a cessation of flight. Finally, entire trials were excluded if the hoverfly was not
456 flying for more than 50% of the trial duration. Head and leg kinematic data were excluded

457 whenever the corresponding WBA data were excluded, ensuring consistent trial inclusion
458 across behavioural metrics.

459 **Visual stimuli**

460 Visual stimuli were generated using custom software
461 (https://github.com/HoverflyLab/FlyFly/releases/tag/v4.2.3) written in MATLAB,
462 incorporating the Psychophysics Toolbox[49,50]. All screens had a refresh rate of 165 Hz and a
463 linearized contrast with a mean illuminance of 200 Lux. For intracellular recordings, the
464 hoverfly was placed 13 cm away from a ViewSonic screen with a resolution of 2560 × 1440
465 pixels, corresponding to 143° × 107° of the visual field. For extracellular recordings, the
466 hoverfly was placed 6.5 cm away from a 2560 × 1440 pixel Asus screen, yielding a projected
467 visual field of 155° × 138° (Supplementary Fig. 6a). For behavioural recordings, the hoverfly
468 was placed 10 cm from a vertically orientated Asus screen (1440 × 2560 pixel,
469 Supplementary Fig. 6b) producing a projected size of 118° × 142°. To evaluate the impact of
470 different screen orientations in electrophysiology and behaviour, visual stimuli were
471 presented either full-screen or using the central 1440 × 1440 pixel square (Supplementary
472 Fig. 6c, d).

473 *Receptive field mapping*

474 To map each neuron's receptive field, we presented local sinusoidal gratings (average
475 38 × 38°) drifting in 8 directions for 0.36 s each, across 48 overlapping locations, as
476 described in detail previously[14]. Stimuli were full contrast, with an average spatial frequency

477 of 0.14 cycles/° and a temporal frequency of 5 Hz. At each location, we calculated the local
478 maximum spike frequency (red, inset, Fig. 1b, e). After subtracting the spontaneous rate,
479 calculated for 0.8 s preceding stimulus onset (dotted line, inset, Fig. 1b, e), we interpolated
480 the resulting local maximum responses to a ten-fold higher spatial resolution (colour coding,
481 Fig. 1a, d). We then quantified the 50% response maximum using Matlab's *contour* function
482 (black, Fig. 1b, e). We created a polygon-shape of this 50% contour line using Matlab's
483 *polyshape* function to calculate the receptive field size, defined as its width and height
484 (Supplementary Fig. 2f), and used the *centroid* function to identify the centre of this
485 polyshape (red circle, Fig. 1b, e). As recordings were performed with the animal ventral side
486 up (Supplementary Fig. 3a, 6a), receptive fields were rotated to display them with the dorsal
487 visual field up.

488 Next, at each location, we fit a cosine function to the responses to the different directions of
489 motion, to extract the local preferred direction (LPD) and local motion sensitivity (LMS;
490 inset, Fig. 1c, f). These were visualized as vectors where angle indicates LPD and length
491 indicates LMS (arrows, Fig. 1a, d). We defined the receptive field preferred direction as the
492 median of LPDs at locations where LMS exceeded 50% of the maximum (black and red
493 arrows; Fig. 1c, f), using *circ_median* from the CircStat toolbox for MATLAB[51]. We
494 calculated the LPD variance using the *circ_var* functions from CircStat toolbox for
495 MATLAB[51], of LPDs at locations where LMS exceeded 50% of the maximum (black and red
496 arrows; Fig. 1c, f).

497 We extracted unpublished receptive field data from 100 reference neurons (other data from
498 five of these optic flow sensitive descending neurons has been published previously[28]) to set
499 exclusion criteria (red shading, Supplementary Fig. 2a, b and c) and to classify the OFS DNs
500 used in the rest of this study. OFS DN1 LHS neurons were defined by receptive field
501 preferred directions between 120° and 200° (light green, Fig. 1g, i). OFS DN1 RHS neurons
502 were defined by receptive field preferred directions between 340° and 60° (dark green, Fig.
503 1g, i). OFS DN2 neurons were classified by receptive field preferred directions between 220°
504 and 320° (yellow and orange, Fig. 1g, i), with the azimuthal location of the receptive field
505 centre determining whether they were LHS or RHS (yellow and orange, Fig. 1h).

506 A polar plot where the distance from origo indicates azimuthal position, and the location
507 along the radius the preferred direction, confirms that the LHS and RHS of OFS1 and OFS2
508 cluster distinctly (Supplementary Fig. 1a). To test whether incorporating additional receptive
509 field parameters would reveal further neuronal subtypes, we performed k-means clustering in
510 Matlab using z-score normalised data. The additional parameters included receptive field
511 centre elevation, receptive field height and width (see Supplementary Fig. 2f), maximum
512 LMS (see Supplementary Fig. 2a), the number of positions with LMS values exceeding 50%
513 of the maximum (see Supplementary Fig. 2b), and LPD variance (see Supplementary Fig.
514 2c). However, the Callinski-Harabasz[52] values indicate that adding additional receptive field
515 parameters actually reduced clustering performance (Supplementary Fig. 1b). In contrast,
516 clustering based solely on preferred direction and azimuthal location yielded four well-
517 defined groups (Supplementary Fig. 1c), and produced the highest Callinski-Harabasz value
518 (Supplementary Fig. 1b).

519 *Directional sensitivity*

520 Full-screen sinusoidal gratings were presented at full contrast, using the same spatial (0.14
521 cycles/°) and temporal (5 Hz) frequencies as in receptive field mapping. For each stimulus
522 direction, mean spike frequency was calculated over the 1 s stimulus duration, excluding the
523 first 100 ms to avoid onset transients[53].We fit a cosine function to the responses to the eight
524 different directions of motion, to extract the preferred direction and response amplitude
525 (Supplementary Fig. 3b), and then plotted these values for OFS DN1 (Supplementary Fig. 3c)
526 and DN2 neurons (Supplementary Fig. 3d). To account for the ventral-side-up recording
527 position (Supplementary Fig. 3a) directional responses were rotated 180° (Supplementary
528 Fig. 3f, g and h). In addition, to display all neurons as RHS, and assuming mirror-symmetry,
529 we flipped LHS neurons across the midline (Supplementary Fig 2i, j, k and l).

530 *Responses to optic flow*

531 We used a starfield stimulus to generate the type of perspective-corrected optic flow that
532 would have been seen by the hoverfly if it was moving through a space of 2 cm diameter
533 spheres (for details, see Ref[14,33]). These simulated translations at 0.5 m/s (sideslip, lift, and
534 thrust) or rotations (pitch, yaw, and roll), at 50°/s. To quantify neural responses, the mean
535 spike frequency was calculated over the 0.97 s stimulus duration, excluding the first 0.1 s to
536 avoid onset-related transients[53]. The spontaneous firing rate, averaged across 0.48 s
537 immediately preceding stimulus onset (open circles, Supplementary Fig 4a, b), was
538 subtracted from the response.

539 *Velocity response functions*

540 We used four types of optic flow: three translations (sideslip, lift and thrust, Supplementary
541 movie 2-7) and one rotation (roll, Supplementary movie 1, 8, 9). Translations were presented
542 at velocities of −2, −1.5, −1, −0.4, −0.2, −0.1, 0, 0.1, 0.2, 0.4, 1, 1.5, and 2 m/s, while
543 rotations were presented at 200, −150, −100, −40, −20, −10, 0, 10, 20, 40, 100, 150, and
544 200°/s. The sign of the velocity indicates the direction of motion as seen by the fly when
545 corrected for its position, with positive values corresponding to counterclockwise roll,
546 leftward sideslip, downward lift, and thrust moving away. Conversely, negative values
547 indicate clockwise roll, rightward sideslip, upward lift, and thrust moving toward the
548 hoverfly. The upper limit was defined by the movement of the individual dots within the
549 starfield stimulus between frames, i.e. was limited by the refresh rate of the screen.

550 Each trial consisted of 39 stimuli (13 unique velocities × 3 repetitions), presented in a random
551 order, with each stimulus lasting 2 s, immediately followed by the next velocity. Trials began
552 with a 1 s blank screen, which served as the pre-stimulation baseline (Fig. 3a and Fig. 5c).
553 Each optic flow condition was repeated multiple times, resulting in at least nine repetitions
554 for each velocity and neuron, and five repetitions for each velocity and animal in behaviour.

555 For neuronal recordings, velocity response function trials were interleaved with the optic
556 flow stimuli described above. In behavioural experiments, a flight refresher sequence
557 interspersed each velocity tuning trial. This consisted of sinusoidal gratings (200°
558 wavelength, 5 Hz) drifting rightward, leftward, and rightward again for 4 s each.

559 Neural responses were quantified as the mean spike frequency during the final second of
560 stimulation (grey shaded areas, Fig. 3a–c). We then calculated the median across trials for
561 each velocity (Fig. 3d). Pre-stimulation activity (spontaneous rate) was measured over a 2 s
562 window immediately preceding stimulus onset. Neural responses are displayed after
563 subtracting the response when viewing a stationary stimulus (filled symbols, Supplementary
564 Fig. 4a, b).

565 In behavioural experiments, we extracted the mean wing beat amplitude of the left and right
566 wings ($\overline{WBA_L}$, $\overline{WBA_R}$, Fig. 5b) during the final second of stimulation (grey shaded areas, in
567 Fig. 5 c, d and e). For each velocity, we calculated the WBA difference (WBAD, defined as
568 $\overline{WBA_L} - \overline{WBA_R}$) and the WBA sum (WBAS, defined as $\overline{WBA_L} + \overline{WBA_R}$, Fig. 5b). We then
569 calculated the median across repetitions for each individual (Fig. 5f). Pre-stimulation
570 responses were averaged over a 0.5 s time window immediately preceding stimulus onset.
571 WBA responses are displayed after subtracting the response when viewing a stationary
572 stimulus (filled symbols, Supplementary Fig. 4c).

573 We defined the head angle as the angle between a straight line joining the 2 tracked points on
574 the head (using *polyfit* in matlab, Fig. 7a, b) and the longitudinal axis of the thorax (Fig. 7a,
575 b). As we filmed in one plane only, this measurement can be caused by a combination of
576 head rotations, but seem to be dominated by roll rotations (Supplementary movie 2-9). We
577 measured the distance between the proximal and distal points of the forelegs (Fig. 7a, c).
578 Note that the forelegs were mostly hidden under the animal from our dorsal view, and could
579 only be seen when extended anteriorly (e.g. Fig. 5a, see also Supplementary movie 2-9). Data

580 are displayed as the mean extension of the left and right foreleg. We measured the distance
581 between the hind leg knee and a lateral point on the mid-abdomen (Fig. 7a, d). Hind leg data
582 are displayed as the mean or the difference of the left and right hind leg. All body parts data
583 are displayed after subtracting the response when viewing a stationary stimulus (filled
584 symbols show hindleg data, Supplementary Fig. 4d).

585 *Response onset*

586 For neuronal recordings, we compared onset times for clockwise roll (+50°/s) and either
587 upwards lift (+0.5 m/s) for OFS DN 1 or downwards lift (-0.5 m/s) for OFS DN2, stimuli
588 which generated strong responses in these neurons (Fig. 3 e, f). Mean spike frequency was
589 calculated over the 0.97 s stimulus duration, excluding the first 0.1 s to avoid onset
590 transients[53]. Onset was defined as the first time point after the first 0.1 s, where spike rate
591 exceeded 80% of the mean.

592 For behaviour, we used WBA responses to roll (-200°/s) and lift (+2 m/s). Mean WBAS was
593 defined as the average response during the final second of stimulation, and onset was defined
594 as the first time point where WBAS exceeded 80% of this mean. We also quantified WBAS,
595 head, fore-and hind leg onsets to sideslip (+2 m/s). For each body part, we quantified the
596 mean response during the final second of stimulation, and onset was defined as the first time
597 point where the response exceeded 80% of this mean.

598

Data availability and statistics

All data and analysis scripts have been submitted to DataDryad (private link for peer review: doi:10.5061/dryad.tb2rbp0fd).

Throughout the text *n* refers to individual repetitions, whereas *N* refers to individual neurons (electrophysiology) or animals (behaviour). All data are presented as median and interquartile range, unless otherwise indicated.

Statistical analyses were performed in Prism 10.4.0 (GraphPad Software), except for circular statistics, which were conducted using the CircStat toolbox for MATLAB[51]. The results of the statistical tests are given in the text, figure legends and in Table 1 and Table 2. For behavioural data the *p*-values were Bonferroni adjusted[54] for multiple comparisons (Table 2).

Acknowledgements

We thank Biomedical Engineering at SAHLN and the Botanic Gardens of Adelaide for their ongoing support. We thank the editor and the two Reviewers for their feedback which greatly improved our paper. This research was funded by the US Air Force Office of Scientific Research (AFOSR, FA9550-19-1-0294 and FA9550-23-1-0473) and the Australian Research Council (ARC, DP210100740, DP230100006 and DP250104770).

Declaration of interests

The authors declare no competing interests.

References

1 Mauss, A. S. & Borst, A. Optic flow-based course control in insects. *Curr Opin Neurobiol* **60**, 21-27, doi:10.1016/j.conb.2019.10.007 (2020).

2 Pierantoni, R. A look into the cock-pit of the fly. The architecture of the lobular plate. *Cell Tissue Res* **171**, 101-122 (1976).

3 Zhao, A. *et al.* A comprehensive neuroanatomical survey of the Drosophila Lobula Plate Tangential Neurons with predictions for their optic flow sensitivity. *bioRxiv*, 2023.2010.2016.562634, doi:10.1101/2023.10.16.562634 (2023).

4 Franz, M. O. & Krapp, H. G. Wide-field, motion-sensitive neurons and matched filters for optic flow fields. *Biol Cybern* **83**, 185-197 (2000).

5 Krapp, H. G., Hengstenberg, B. & Hengstenberg, R. Dendritic structure and receptive-field organization of optic flow processing interneurons in the fly. *J Neurophysiol* **79**, 1902-1917. (1998).

6 Wei, H., Kyung, H. Y., Kim, P. J. & Desplan, C. The diversity of lobula plate tangential cells (LPTCs) in the Drosophila motion vision system. *Journal of Comparative Physiology A* **206**, 139-148, doi:10.1007/s00359-019-01380-y (2020).

7 Strausfeld, N. J. & Bassemir, U. K. Lobula plate and ocellar interneurons converge onto a cluster of descending neurons leading to neck and leg neuropil in *Calliphora erythrocephala*. *Cell Tissue Res* **240**, 617-640 (1985).

8 Strausfeld, N. J. & Seyan, H. S. Convergence of visual, haltere, and prosternai inputs at neck motor neurons of *Calliphora erythrocephala*. *Cell and Tissue Research* **240**, 601-615 (1985).

9 Namiki, S., Dickinson, M. H., Wong, A. M., Korff, W. & Card, G. M. The functional organization of descending sensory-motor pathways in *Drosophila*. *eLife* **7**, e34272, doi:10.7554/eLife.34272 (2018).

10 Suver, M. P., Huda, A., Iwasaki, N., Safarik, S. & Dickinson, M. H. An Array of Descending Visual Interneurons Encoding Self-Motion in Drosophila. *J Neurosci* **36**, 11768-11780, doi:10.1523/JNEUROSCI.2277-16.2016 (2016).

11 Erginkaya, M. *et al.* A competitive disinhibitory network for robust optic flow processing in Drosophila. *bioRxiv*, 2023.2008.2006.552150, doi:10.1101/2023.08.06.552150 (2023).

12 Haikala, V., Joesch, M., Borst, A. & Mauss, A. S. Optogenetic control of fly optomotor responses. *J Neurosci* **33**, 13927-13934, doi:10.1523/jneurosci.0340-13.2013 (2013).

13 Pokusaeva, V. O., Satapathy, R., Symonova, O. & Joesch, M. Bilateral interactions of optic-flow sensitive neurons coordinate course control in flies. *Nat Commun* **15**, 8830, doi:10.1038/s41467-024-53173-w (2024).

14 Nicholas, S., Leibbrandt, R. & Nordström, K. Visual motion sensitivity in descending neurons in the hoverfly. *J Comp Physiol A* **206**, 149-163, doi:10.1007/s00359-020-01402-0 (2020).

15 Haag, J., Wertz, A. & Borst, A. Integration of lobula plate output signals by DNOVS1, an identified premotor descending neuron. *J Neurosci* **27**, 1992-2000, doi:10.1523/jneurosci.4393-06.2007 (2007).

16 Wertz, A., Borst, A. & Haag, J. Nonlinear integration of binocular optic flow by DNOVS2, a descending neuron of the fly. *J Neurosci* **28**, 3131-3140, doi:10.1523/jneurosci.5460-07.2008 (2008).

17 Collett, T. S. & Land, M. F. Visual control of flight behaviour in the hoverfly, *Syritta pipiens* L. *J Comp Physiol A* **99**, 1-66 (1975).

18 Wellington, W. & Fitzpatrick, S. Territoriality in the drone fly, *Eristalis tenax* (Diptera, Syrphidae). *Can Entomol* **113**, 695-704 (1981).

19 Collett, T. S. & Land, M. F. How hoverflies compute interception courses. *Journal of comparative physiology* **125**, 191-204, doi:10.1007/BF00656597 (1978).

20 Dankova, K., Nicholas, S. & Nordstrom, K. Temperature during pupal development affects hoverfly developmental time, adult life span, and wing length. *Ecol Evol* **13**, e10516, doi:10.1002/ece3.10516 (2023).

21 Nicholas, S., Thyselius, M., Holden, M. & Nordström, K. Rearing and long-term maintenance of *Eristalis tenax* hoverflies for research studies. *JoVE*, e57711, doi:doi:10.3791/57711 (2018).

22 Dudley, R. Mechanisms and implications of animal flight maneuverability. *Integr Comp Biol* **42**, 135-140, doi:10.1093/icb/42.1.135 (2002).

23 Straw, A. D., Warrant, E. J. & O'Carroll, D. C. A 'bright zone' in male hoverfly (*Eristalis tenax*) eyes and associated faster motion detection and increased contrast sensitivity. *J Exp Biol* **209**, 4339-4354, doi:10.1242/jeb.02517 (2006).

24 van Hateren, J. H., Hardie, R. C., Rudolph, A., Laughlin, S. B. & Stavenga, D. G. The bright zone, a specialized dorsal eye region in the male blowfly *Chrysomyia megacephala*. *J Comp Physiol A* **164**, 297-308 (1989).

25 Hornstein, E. P., O'Carroll, D. C., Anderson, J. C. & Laughlin, S. B. Sexual dimorphism matches photoreceptor performance to behavioural requirements. *Proc R Soc Lond B Biol Sci* **267**, 2111-2117., doi:10.1098/rspb.200.1257 (2000).

26 Nordström, K., Barnett, P. D., Moyer de Miguel, I. M., Brinkworth, R. S. A. & O'Carroll, D. C. Sexual dimorphism in the hoverfly motion vision pathway. *Curr Biol* **18**, 661-667, doi:10.1016/j.cub.2008.03.061 (2008).

27 Barnett, P. D., Nordström, K. & O'Carroll, D. C. Motion adaptation and the velocity coding of natural scenes. *Curr Biol* **20**, 994-999, doi:10.1016/j.cub.2010.03.072 (2010).

28 Nicholas, S. & Nordström, K. Facilitation of neural responses to targets moving against optic flow. *Proc Natl Acad Sci U S A* **118**, doi:10.1073/pnas.2024966118 (2021).

29 Ghosh, A., Nicholas, S., Nordström, K., Nowotny, T. & Knight, J. Understanding the mechanism of facilitation in hoverfly TSDNs. *PLOS Computational Biology* **21**, e1012986, doi:10.1371/journal.pcbi.1012986 (2025).

30 Nicholas, S., Supple, J., Leibbrandt, R., Gonzalez-Bellido, P. T. & Nordström, K. Integration of small- and wide-field visual features in Target-Selective Descending Neurons of both predatory and non-predatory dipterans. *J Neurosci* **38**, 10725-10733, doi:10.1523/jneurosci.1695-18.2018 (2018).

31 Thyselius, M., Gonzalez-Bellido, P. T., Wardill, T. J. & Nordstrom, K. Visual approach computation in feeding hoverflies. *J Exp Biol* **221**, doi:10.1242/jeb.177162 (2018).

32 Thyselius, M. *et al.* Hoverfly (Eristalis tenax) pursuit of artificial targets. *J Exp Biol* **226**, doi:10.1242/jeb.244895 (2023).

33 Leibbrandt, R., Nicholas, S. & Nordström, K. The impulse response of optic flow-sensitive descending neurons to roll m-sequences. *J Exp Biol* **224**, doi:10.1242/jeb.242833 (2021).

34 Suver, M. P., Huda, A., Iwasaki, N., Safarik, S. & Dickinson, M. H. An array of descending visual interneurons encoding self-motion in *Drosophila*. *J Neurosci* **36**, 11768 (2016).

35 Mathis, A. *et al.* DeepLabCut: markerless pose estimation of user-defined body parts with deep learning. *Nat Neurosci* **21**, 1281-1289, doi:10.1038/s41593-018-0209-y (2018).

36 Ogawa, Y. *et al.* Combining Unity with machine vision to create low latency, flexible and simple virtual realities. *Methods in Ecology and Evolution* **16**, 126-144, doi:https://doi.org/10.1111/2041-210X.14449 (2025).

37 Götz, K. G. Flight control in *Drosophila* by visual perception of motion. *Kybernetik* **4**, 199-208 (1968).

38 Maimon, G., Straw, A. D. & Dickinson, M. H. Active flight increases the gain of visual motion processing in *Drosophila*. *Nat Neurosci* **13**, 393-399, doi:nn.2492 [pii] 10.1038/nn.2492 [doi] (2010).

39 Tammero, L. F., Frye, M. A. & Dickinson, M. H. Spatial organization of visuomotor reflexes in Drosophila. *J Exp Biol* **207**, 113-122, doi:10.1242/jeb.00724 (2004).

40 Ristroph, L. *et al.* Discovering the flight autostabilizer of fruit flies by inducing aerial stumbles. *Proc Natl Acad Sci U S A* **107**, 4820-4824, doi:10.1073/pnas.1000615107 (2010).

41 Schnell, B., Weir, P. T., Roth, E., Fairhall, A. L. & Dickinson, M. H. Cellular mechanisms for integral feedback in visually guided behavior. *Proc Natl Acad Sci U S A* **111**, 5700-5705, doi:1400698111 [pii] 10.1073/pnas.1400698111 [doi] (2014).

42 Theobald, J. C., Ringach, D. L. & Frye, M. A. Dynamics of optomotor responses in *Drosophila* to perturbations in optic flow. *J Exp Biol* **213**, 1366-1375, doi:213/8/1366 [pii] 10.1242/jeb.037945 [doi] (2010).

43 Nicholas, S., Ogawa, Y. & Nordström, K. Dual receptive fields underlying target and wide-field motion sensitivity in looming-sensitive descending neurons. *eNeuro* **10**, ENEURO.0188-0123.2023, doi:10.1523/eneuro.0188-23.2023 (2023).

44 Kim, A. J., Fenk, L. M., Lyu, C. & Maimon, G. Quantitative Predictions Orchestrate Visual Signaling in Drosophila. *Cell* **168**, 280-294 e212, doi:10.1016/j.cell.2016.12.005 (2017).

45 Zanker, J. M. The Wing Beat of Drosophila-Melanogaster .3. Control. *Philos T R Soc B* **327**, 45-64, doi:DOI 10.1098/rstb.1990.0042 (1990).

46 Sane, S. P. The aerodynamics of insect flight. *Journal of Experimental Biology* **206**, 4191-4208, doi:10.1242/jeb.00663 (2003).

47 Niven, J. E. & Scharlemann, J. P. W. Do insect metabolic rates at rest and during flight scale with body mass? *Biol Letters* **1**, 346-349, doi:10.1098/rsbl.2005.0311 (2005).

48 Schneider, C. A., Rasband, W. S. & Eliceiri, K. W. NIH Image to ImageJ: 25 years of image analysis. *Nat Methods* **9**, 671-675, doi:10.1038/nmeth.2089 (2012).

49 Brainard, D. H. The Psychophysics Toolbox. *Spat Vis* **10**, 433-436 (1997).

50 Pelli, D. G. The VideoToolbox software for visual psychophysics: transforming numbers into movies. *Spat Vis* **10**, 437-442 (1997).

51 Berens, P. CircStat: A MATLAB toolbox for circular statistics. *Journal of Statistical Software* **31**, 1 - 21, doi:10.18637/jss.v031.i10 (2009).

52 Caliński, T. & Harabasz, J. A dendrite method for cluster analysis. *Communications in Statistics* **3**, 1-27, doi:10.1080/03610927408827101 (1974).

53 Nicholas, S. & Nordstrom, K. Persistent Firing and Adaptation in Optic-Flow-Sensitive Descending Neurons. *Curr Biol* **30**, 2739-2748 e2732, doi:10.1016/j.cub.2020.05.019 (2020).

54 Abdi, H. in *Encyclopedia of measurement and statistics* (ed N. J. Salkind) (Sage, 2007).

55 Kane, G. A., Lopes, G., Saunders, J. L., Mathis, A. & Mathis, M. W. Real-time, low-latency closed-loop feedback using markerless posture tracking. *eLife* **9**, doi:10.7554/eLife.61909 (2020).

770 ## Figure legends

771 **Fig. 1. Classification of optic flow sensitive (OFS) descending neurons (DN) in *Eristalis***
772 ***tenax*. a** Receptive field of a representative OFS DN1 recorded from a male hoverfly. Colour
773 coding indicates the local maximum spike frequency (red, inset, panel b), the direction of the
774 arrows shows the local preferred direction (LPD, red arrowhead, panel c) and their length the
775 local motion sensitivity (LMS, red, panel c). As the stimuli were not perspective corrected,
776 the receptive field map reflects the visual monitor. **b** Contour line representing the 50%
777 receptive field boundary based on local maximum spike frequency (colour coding, panel a).
778 Inset: example response at one central location to eight directions of motion (black circles),
779 showing local maximum spike frequency (local max, red line) above spontaneous rate (spont,
780 black dotted line). **c** Local preferred direction (LPD) map of the same example neuron at
781 locations where local motion sensitivity (LMS) exceeds 50% of the maximum. Inset:
782 example response at one location to eight directions of motion with a sinusoidal fit (black
783 line), illustrating LMS (red line) and LPD (red arrowhead). The data in the inset corresponds
784 to the red arrow. **d** Receptive field of a representative male OFS DN2. **e** 50% receptive field
785 contour and receptive field centre of the neuron shown in panel d. **f** Preferred direction map
786 of the same OFS DN2. **g** Distribution of receptive field preferred directions across 100 male
787 reference neurons, colour-coded by neuron classification. Dashed lines in corresponding
788 colours indicate the thresholds used for neuron type classification. **h** Receptive field centres
789 of the same 100 reference neurons, using the same colour coding. **i** Relationship between
790 preferred direction and receptive field centre for the 100 neurons. Note that the scale is the

same for the azimuth and elevation, and the scale bar in panels a, d, h and i correspond to both the x- and y-axis.

Fig. 2. Sex-based comparison of direction sensitivity in OFS DNs. a Polar plot showing the preferred direction of male (blue) and female (red) OFS DNs in response to a full-screen, full-contrast sinusoidal grating (spatial wavelength 7º, temporal frequency 5 Hz) moving in eight different directions (see also Supplementary Fig. 3). Individual data points represent the response amplitude and preferred direction of each OFS DN (red, Supplementary Fig. 3j). Larger, salient circles indicate the population median, with error bars showing the interquartile range. The dashed lines indicate the directional thresholds used to classify neuron type, as OFS DN1 (male: N = 9; female: N = 12) or OFS DN2 (male: N = 20; female: N = 14). Asterisk indicates a statistically significant difference ($p < 0.05$, Watson-Williams two-sample test). **b** Comparison of male and female OFS DN1 responses to translational optic flow at 0.5 m/s: sideslip, lift and thrust; and rotational optic flow at 50 º/s: pitch, yaw and roll (male: N = 9; female: N = 12). **c** Comparison of male and female OFS DN2 responses to the same optic flow stimuli (male: N = 20; female: N = 14). Data presented as median and interquartile range.

Fig. 3. Velocity response functions in male and female OFS DNs. a Example stimulus profile over time, with roll velocity on the y-axis. **b** Representative spike histogram from a single trial from a male OFS DN2, smoothed using a 100 ms square-wave filter with 0.025 ms resolution, and time-aligned to the stimulus shown in panel a. Grey shading in panels a and b highlight the analysis windows used to calculate response. **c** Example extracellular raw

812 data traces extracted from the analysis windows in panel b, illustrating neuronal responses to
813 roll velocities of –150, 10, and 200 º/s. **d** Average spike frequency (grey circles) was
814 calculated for each repetition from each neuron (N = 1 neuron, n = 18 repetitions), and the
815 median of these (black) was used for further analysis. **e** Velocity response functions of OFS
816 DN1 in male (blue) and female (red) hoverflies in response to roll (N = 4 males, 5 females),
817 sideslip (N = 5, 6), lift (N = 4, 4), and thrust (N = 3, 5). **f** Velocity response functions of OFS
818 DN2 to roll (N = 10 males, 8 females), sideslip (N = 6, 7), lift (N = 6, 7), and thrust (N = 6,
819 7). Data in panels e and f are presented as median and interquartile range. Asterisks indicate
820 statistically significant differences, two-way ANOVA with Šídák's multiple comparisons test
821 (** $p < 0.01$ and **** $p < 0.0001$), see also Table 1.

822 **Fig. 4. Morphological reconstruction of OFS DNs. a** Schematic diagram of the hoverfly
823 central brain and thoracic ganglia showing the projections of OFS DN1 (green) and OFS
824 DN2 (orange). Key anatomical landmarks are labelled: CB, central brain; OL, optic lobe; CC,
825 cervical connective; T1 LN, prothoracic leg nerve; T2 LN, mesothoracic leg nerve; T3 LN,
826 metathoracic leg nerve; TAG, thoracic-abdominal ganglion; FN, frontal nerve; PtN,
827 pterothoracic nerve; HN, haltere nerve; AbN, abdominal nerve. **b** Confocal image of a
828 reconstructed male OFS DN2. White boxes indicate regions magnified in panels d - i. **c** A
829 magnification of the thoracic ganglion in panel b. **d** Input dendrites of the same OFS DN2
830 around the sub-oesophageal ganglion. **e** Input dendrites of a female OFS DN2. **f** Input
831 dendrites of a male OFS DN1. **g** Output projections of the same OFS DN2 neuron as in
832 panels b, c and d. **f** Output projections within the thoracic ganglia of the neuron in panel e. **h**
833 Output projections of the neuron in panel f.

834 **Fig. 5. WBA velocity response functions in male and female hoverflies. a** A single frame
835 from a video labelled with trained DeepLabCut models[35,36,55]. Coloured dots correspond to
836 those in panel b, used to extract the wing beat amplitude (WBA). **b** Pictogram illustrating a
837 higher wing beat amplitude on the left wing (WBA_L) compared to the right wing (WBA_R),
838 suggesting a turn to the right. Equations used to calculate wing beat amplitude difference
839 (WBAD) and wing beat amplitude sum (WBAS). **c** Example stimulus with sideslip velocity
840 on the y-axis. **d** Representative WBA for the left (pale colour) and right (salient colour)
841 wings from a single trial, time-aligned with the stimulus shown in panel c. Grey shading in
842 panels c and d indicate the analysis windows used to calculate WBAD and WBAS. **e**
843 Magnified view of example WBA, showing behavioural responses to sideslip velocities of -2,
844 0.2, and 2 m/s. **f** Average WBAS (grey circles) calculated across repetitions (N = 1 animal,
845 n = 19-36 repetitions). Black circles represent the median WBAS per stimulus velocity, used
846 for further analysis. **g** WBAD in male (blue) and female (red) hoverflies in response to
847 different optic flow velocities: roll (N = 5 males, 7 females), sideslip (N = 6, 6), lift (N = 7,
848 5), and thrust (N = 6, 5). **h** WBAS to the same stimuli in the same animals. Data in panels g
849 and h are presented as median and interquartile range.

850 **Fig. 6. Response onset to roll and lift stimuli in male and female hoverflies. a** Time to
851 response onset in OFS DN1 to roll (+50 °/s) or lift (+0.5 m/s) stimuli in males (blue, N = 5)
852 and females (red, N = 8). **b** Response onset in OFS DN2 to roll (+50 °/s) or lift (-0.5 m/s)
853 measured in males (N = 20) and females (N = 14). **c** Onset of WBAS responses to roll
854 (-200 °/s) and lift (+2 m/s) in males (N = 5 for roll, 9 for lift) and females (N = 7 for roll, 5
855 for lift). Data are presented from individual neurons (a, b) or animals (c) with lines indicating

median. Asterisks indicate statistically significant differences, two-way ANOVA with uncorrected Fisher's LSD test (** $p < 0.01$ and *** $p < 0.001$).

Fig. 7. Velocity response functions of the head, fore- and hind legs in male and female hoverflies. a A single frame highlighting the points used to track the head (yellow and dark green), thorax (orange), forelegs (pale and dark blue), and hind legs (magenta and pale green). **b** The head angle (HA) was defined as the angle between the medio-posterior head and the longitudinal thorax axis. **c** The foreleg extension was defined as the distance between the proximal and distal point, after calculating the average for the left and the right leg. **d** The hind leg extension was defined as the distance between the knee and a lateral point on the mid-abdomen, after calculating the average for the left and the right leg. We also calculated the difference between the right and the left hind leg. **e** The head angle in male (blue) and female (red) hoverflies in response to different optic flow velocities: roll (N = 5 males, 7 females), sideslip (N = 6, 6), lift (N = 7, 5), and thrust (N = 6, 5). **f** The foreleg extension to the same stimuli in the same animals. **g** The hind leg extension in the same animals. **h** The difference between the left and right hind leg extension in the same animals. The data in panels e, f, g and h are presented as median and interquartile range. Asterisks indicate statistically significant differences, two-way ANOVA with Šídák's multiple comparisons test (* $p < 0.05$, ** $p < 0.01$), see also Table 2.

Table legends

Table 1. Statistical summary of neural velocity response functions. Results from two-way ANOVA analyses evaluating the effects of stimulus velocity and sex on neural responses

877 (OFS DN1 and DN2). Asterisks denote levels of statistical significance:

878 *** $p < 0.001$, **** $p < 0.0001$.

879 **Table 2. Statistical summary of behavioural velocity response functions.** Results from

880 two-way ANOVA analyses evaluating the effects of stimulus velocity and sex on behavioural

881 responses (WBAS, WBAD, head angle, foreleg extension, hind leg extension and hind leg

882 difference). Asterisks denote levels of statistical significance: ** $p < 0.01$,

883 *** $p < 0.001$, **** $p < 0.0001$, after performing a Bonferroni correction[54] for 6 comparisons

884 of data from the same videos.

885

Figure 1

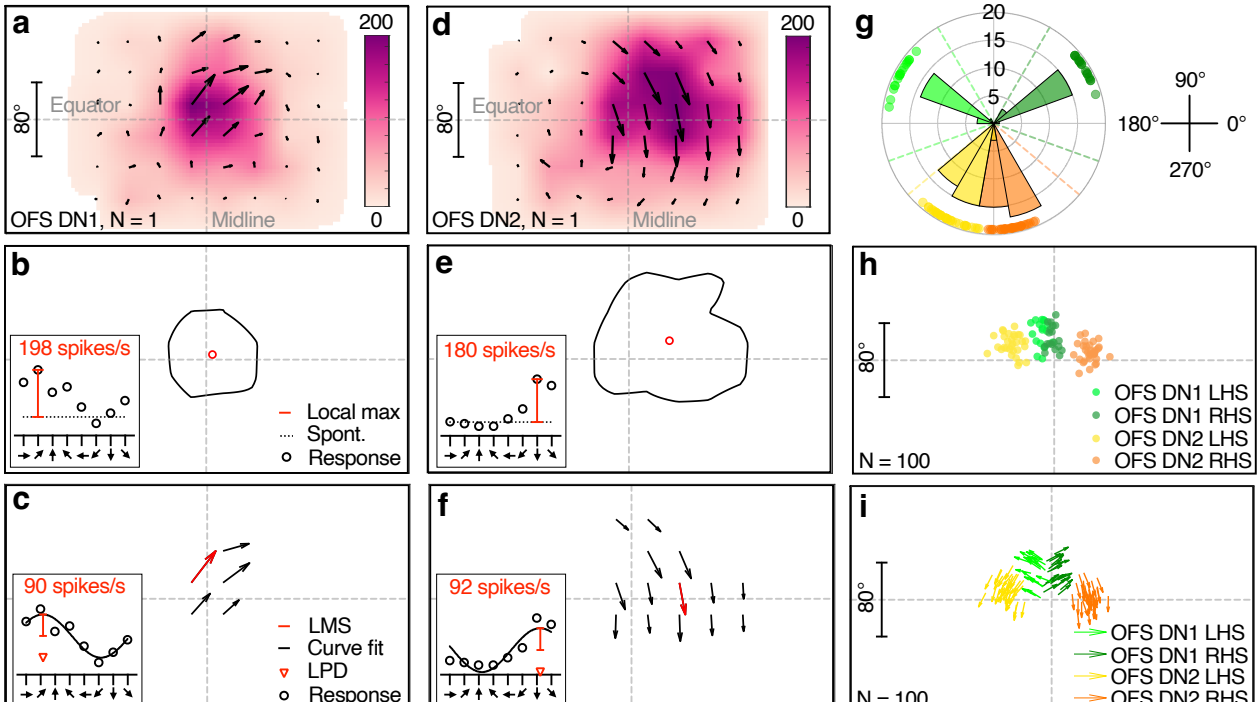
a
200
0
80°
Equator
OFS DN1, N = 1
Midline
d
200
0
80°
Equator
OFS DN2, N = 1
Midline
g
20
15
10
5
90°
180°
0°
270°
b
198 spikes/s
Local max
Spont.
Response
e
180 spikes/s
h
80°
OFS DN1 LHS
OFS DN1 RHS
OFS DN2 LHS
OFS DN2 RHS
N = 100
c
90 spikes/s
LMS
Curve fit
LPD
Response
f
92 spikes/s
i
80°
OFS DN1 LHS
OFS DN1 RHS
OFS DN2 LHS
OFS DN2 RHS
N = 100

Figure 2

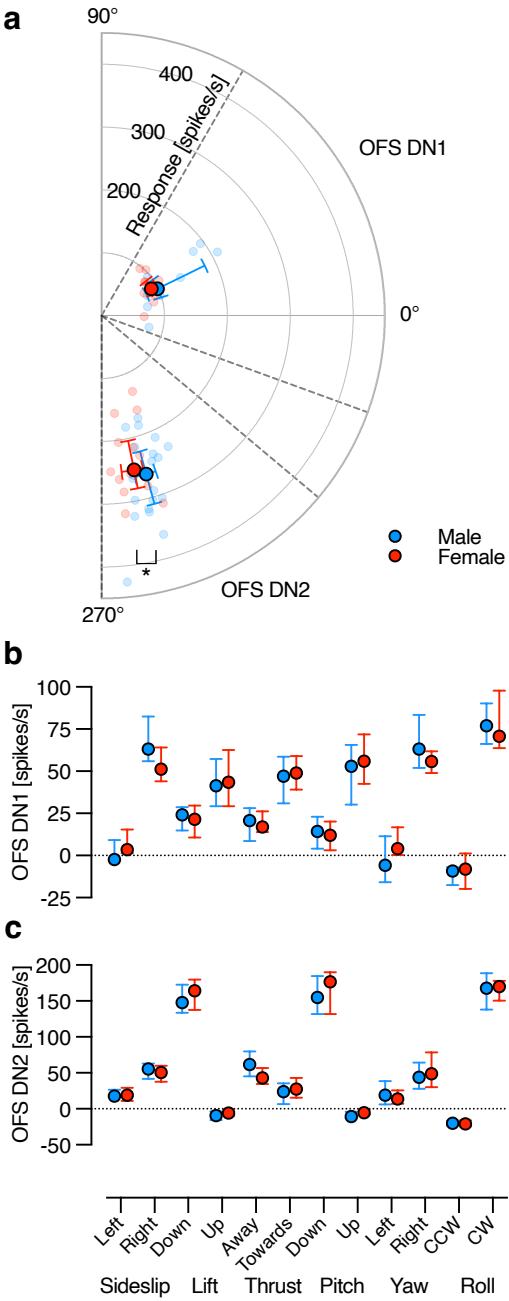
a
90°
400
300
200
Response [spikes/s]
OFS DN1
0°
Male
Female
*
OFS DN2
270°
b
OFS DN1 [spikes/s]
100
75
50
25
0
-25
c
OFS DN2 [spikes/s]
200
150
100
50
0
-50
Left
Right
Down
Up
Away
Towards
Down
Up
Left
Right
CCW
CW
Sideslip
Lift
Thrust
Pitch
Yaw
Roll

Figure 3

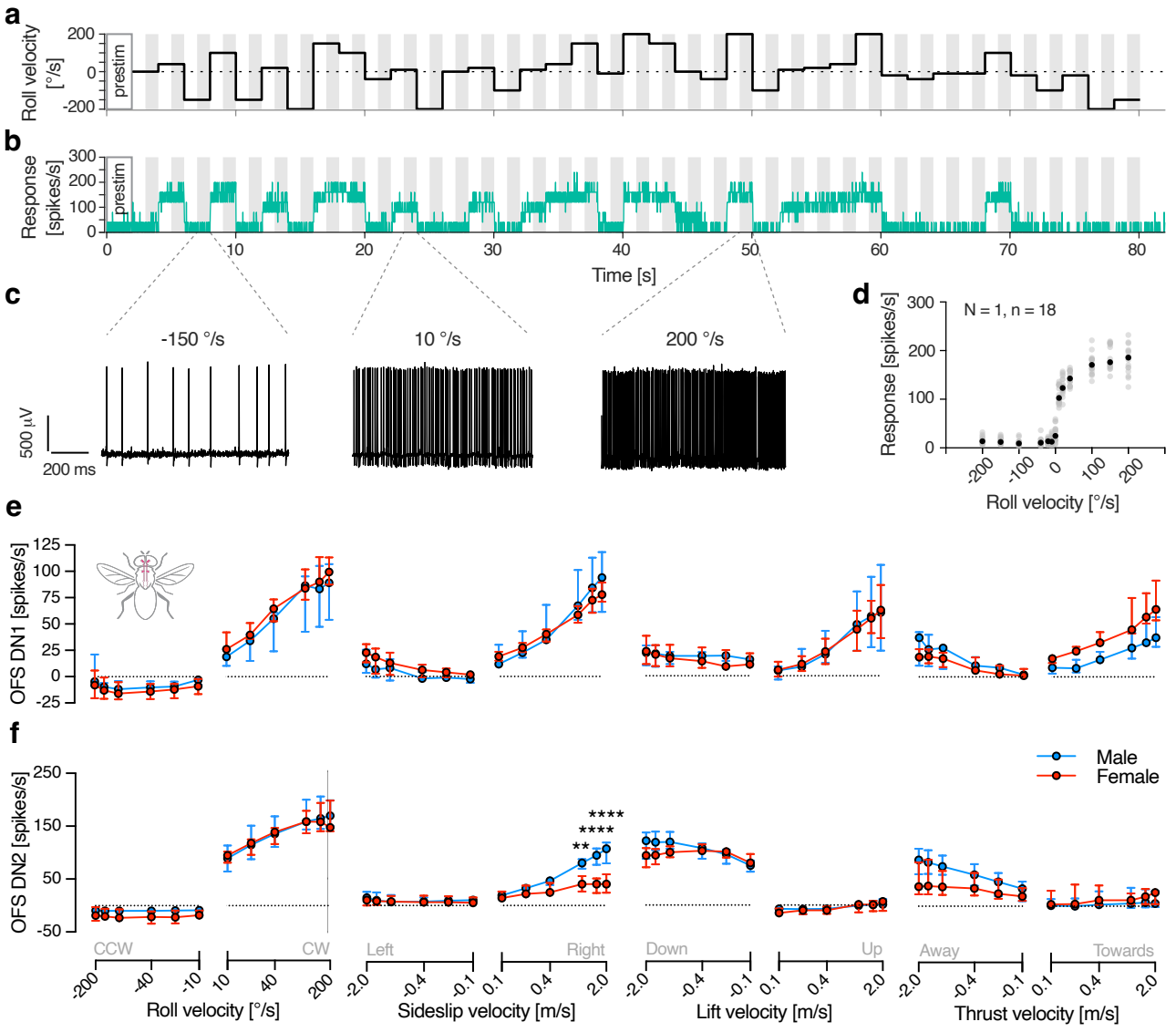
a
Roll velocity [°/s]
200
0
-200
prestim
b
Response [spikes/s]
300
200
100
0
prestim
0
10
20
30
40
50
60
70
80
Time [s]
c
-150 °/s
10 °/s
200 °/s
500 µV
200 ms
d
N = 1, n = 18
Response [spikes/s]
300
200
100
0
-200
-100
0
100
200
Roll velocity [°/s]
e
OFS DN1 [spikes/s]
125
100
75
50
25
0
-25
f
OFS DN2 [spikes/s]
250
150
50
-50
Male
Female
****
****
**
CCW
CW
Left
Right
Down
Up
Away
Towards
-200
-40
-10
10
40
200
Roll velocity [°/s]
-2.0
-0.4
-0.1
0.1
0.4
2.0
Sideslip velocity [m/s]
Lift velocity [m/s]
Thrust velocity [m/s]

Figure 4

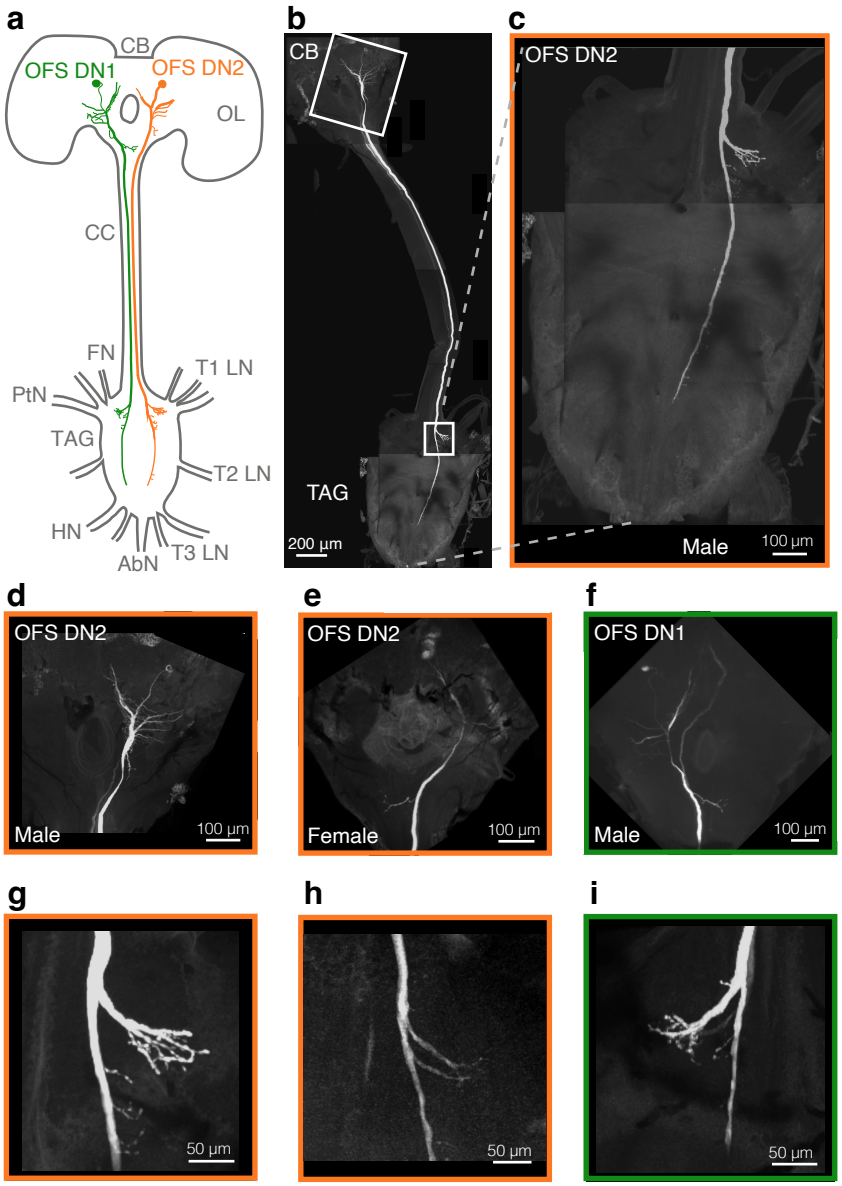
a
CB
OFS DN1
OFS DN2
OL
CC
FN
T1 LN
PtN
TAG
T2 LN
HN
AbN
T3 LN
b
CB
TAG
200 µm
c
OFS DN2
Male
100 µm
d
OFS DN2
Male
100 µm
e
OFS DN2
Female
100 µm
f
OFS DN1
Male
100 µm
g
50 µm
h
50 µm
i
50 µm

Figure 5

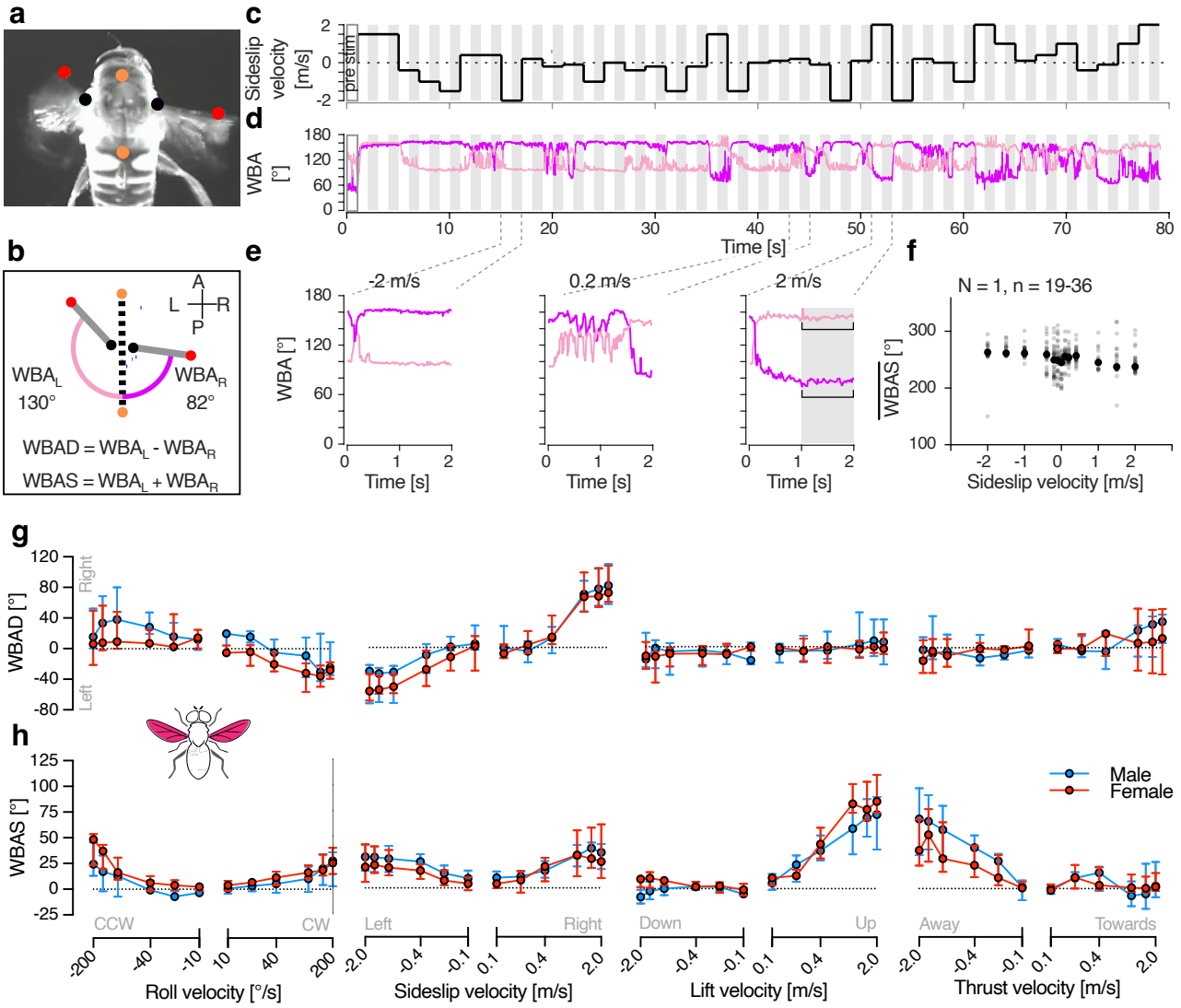
a
b
c
d
e
f
g
h
Sideslip velocity [m/s]
pre stim
WBA [°]
Time [s]
-2 m/s
0.2 m/s
2 m/s
A
L
R
P
WBA_L
130°
WBA_R
82°
WBAD = WBA_L - WBA_R
WBAS = WBA_L + WBA_R
N = 1, n = 19-36
WBAS [°]
Sideslip velocity [m/s]
WBAD [°]
Right
Left
Male
Female
CCW
CW
Left
Right
Down
Up
Away
Towards
Roll velocity [°/s]
Sideslip velocity [m/s]
Lift velocity [m/s]
Thrust velocity [m/s]

Figure 6

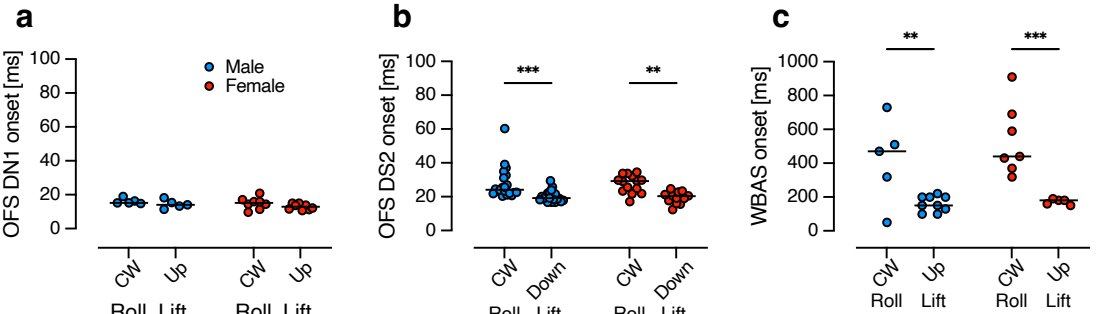
a
OFS DN1 onset [ms]
100
80
60
40
20
0
Male
Female
CW
Up
CW
Up
Roll
Lift
Roll
Lift
b
OFS DS2 onset [ms]
100
80
60
40
20
0
***
**
CW
Down
CW
Down
Roll
Lift
Roll
Lift
c
WBAS onset [ms]
1000
800
600
400
200
0
**
***
CW
Up
CW
Up
Roll
Lift
Roll
Lift

Figure 7

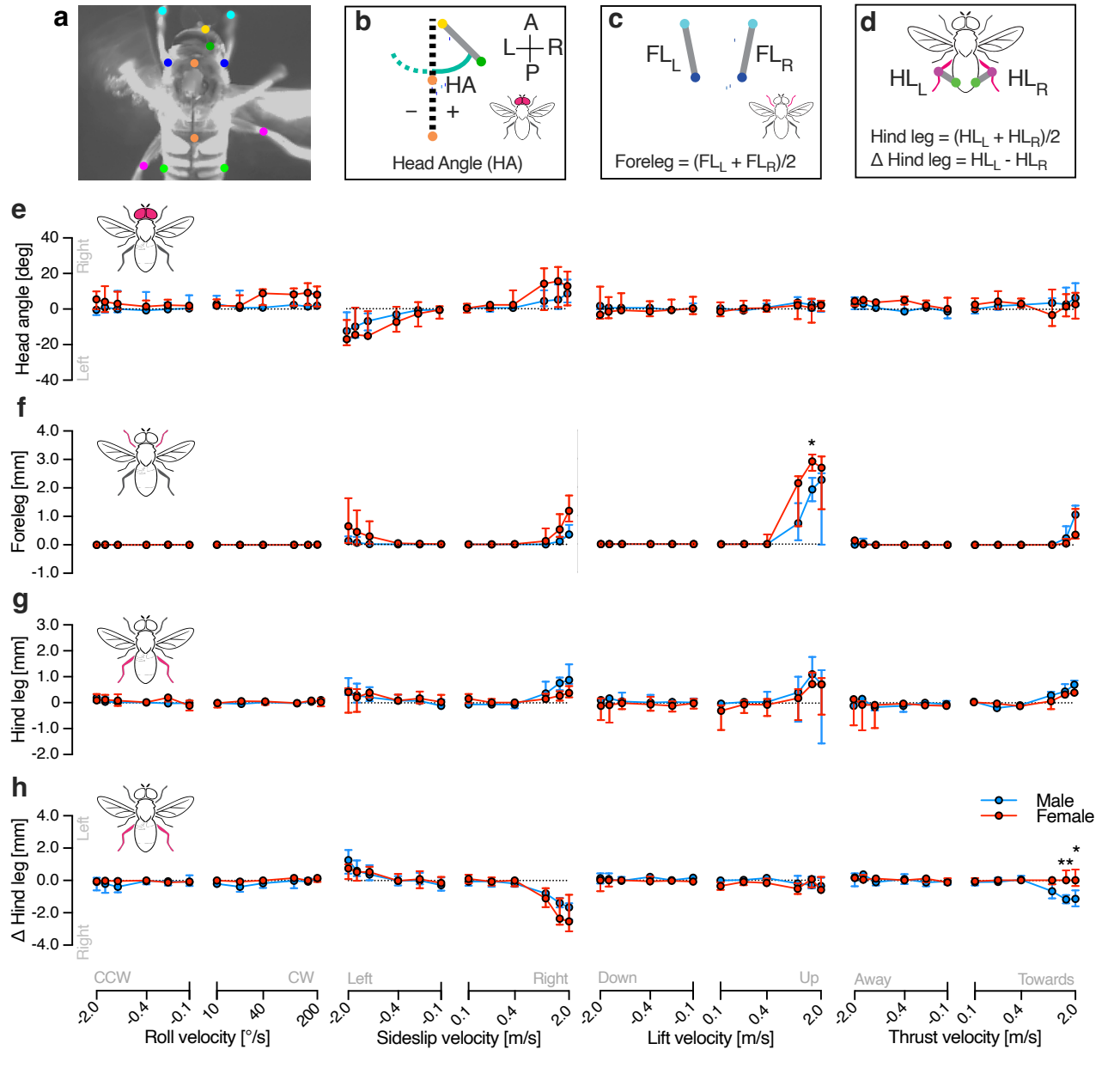
a
b
A
L
R
P
HA
−
+
Head Angle (HA)
c
FL_L
FL_R
Foreleg = (FL_L + FL_R)/2
d
HL_L
HL_R
Hind leg = (HL_L + HL_R)/2
Δ Hind leg = HL_L - HL_R
e
Head angle [deg]
Right
Left
f
Foreleg [mm]
g
Hind leg [mm]
h
Δ Hind leg [mm]
Left
Right
Male
Female
CCW
CW
Left
Right
Down
Up
Away
Towards
Roll velocity [°/s]
Sideslip velocity [m/s]
Lift velocity [m/s]
Thrust velocity [m/s]

Table 1

Stimulus		Velocity	Sex	Interaction		Velocity	Sex	Interaction
Roll	OFS DN1	****	0.35	0.14	OFS DN2	****	0.31	>0.99
Sideslip		****	0.90	0.12		****	**0.01**	****
Lift		**0.002**	0.86	>0.99		****	0.18	***
Thrust		****	0.11	****		****	0.10	**0.02**

Table 2

Stimulus		Velocity	Sex	Interaction		Velocity	Sex	Interaction
Roll	WBAD	****	0.66	>0.99	WBAS	****	0.78	>0.99
Sideslip		****	>0.99	>0.99		****	>0.99	>0.99
Lift		0.18	>0.99	>0.99		****	0.54	0.12
Thrust		>0.99	>0.99	>0.99		**	>0.99	>0.99
Roll	Head	0.94	>0.99	>0.99	Foreleg	0.89	>0.99	0.26
Sideslip		**	>0.99	>0.99		**	**0.04**	**0.01**
Lift		>0.99	>0.99	>0.99		****	0.38	**0.03**
Thrust		>0.99	>0.99	0.08		**	>0.99	>0.99
Roll	Hind leg	0.21	>0.99	0.17	Δ Hind leg	**	>0.99	**0.02**
Sideslip		**0.04**	>0.99	**0.02**		****	>0.99	>0.99
Lift		0.39	>0.99	>0.99		0.41	>0.99	>0.99
Thrust		0.07	>0.99	>0.99		**	0.06	****

Supplementary information

Sexual dimorphism in sensorimotor transformation of optic flow

Sarah Nicholas[1], Katja Sporar Klinge[1#], Luke Turnbull[1], Annabel Moran[1], Aika Young[1], Yuri Ogawa[1], Karin Nordström[1,2*]*

Supplementary Figure legends

Supplementary Fig 1. a The four clusters as identified by us (see Fig. 1g, h and i) displayed on a polar plot where the distance from origo illustrates the azimuthal position and the position along the circumference the preferred direction, colour coded as in the main paper (pale green: OFS DN1 LHS; dark green: OFS DN1 RHS; yellow: OFS DN2 LHS; orange: OFS DN2 RHS). **b** The Calinski-Harabasz value[1] as a function of cluster number when using only the azimuthal location of the receptive field centre and the preferred direction (red), or when adding one other receptive field criterion (grey, receptive field centre elevation, receptive field height or width, maximum LMS, the number of positions with LMS values exceeding 50% of the maximum, or LPD variance, see Methods), or all receptive field criteria (blue). **c** The resulting z-score for azimuthal location and preferred direction, and the four clusters using k-means clustering in Matlab.

Supplementary Fig 2. Exclusion criteria and receptive field comparisons in male and female OFS DNs. a Distribution of maximum local motion sensitivity (LMS) in 100 male reference neurons (grey histogram, N = 100) compared to the neurons used for quantification in the rest of the paper (N = 35 males, 36 females). Six neurons with a maximum LMS below 20 spikes/s (red cross-hatched region or dashed line) were excluded from further analysis. **b** Number of stimulus positions with LMS greater than 50% of the neuron's maximum LMS (black and red arrows in Fig. 1c and f). Neurons with fewer than 4 positions were excluded.

c Distribution of LPD variance. Neurons with directional variance exceeding 30° were excluded. **d** Classification of male neurons based on receptive field centre and preferred direction. The top panel shows the preferred directions across neurons, with dashed lines indicating the directional thresholds used for neuron type classification. The middle panel shows receptive field centre locations, and the bottom panel illustrates the relationship between receptive field centre and the receptive field preferred direction for all 35 male neurons, with 2 neurons excluded from further analysis (grey). Note that the scale is the same for the azimuth and elevation, and the scale bar corresponds to both the x- and y-axis. **e** Same classification criteria applied to 36 female neurons, with 7 neurons excluded (grey). **f** The receptive field width and height at the 50% contour line for the remaining OFS DN 1 (N = 10 males, 12 females) and OFS DN2 (N = 23 males, 17 females). Individual data points from independent neurons, with black lines representing the median.

Supplementary Fig 3. Schematic illustration showing the steps used to standardize data across recordings. a. Top panel, ventral-side-up position of hoverfly during electrophysiology recordings. **b** Response of an example OFS DN2 neuron to a full-screen, full-contrast sinusoidal grating (spatial wavelength 7°; temporal frequency 5 Hz) moving in eight different directions. The red arrowhead shows the neuron's preferred direction, and the red line indicates response amplitude. **c** Preferred direction of male hoverfly OFS DNs (N = 29). Neurons are colour coded by classification. **d** Preferred direction of female hoverfly OFS DNs (N = 26). Neurons are colour coded by classification. **e** We rotated the data 180° to display the dorsal visual field up. **f** Direction sensitivity of the same neuron as in panel b after rotating the data 180°. **g** Preferred direction of male hoverfly OFS DNs after rotating the data 180°. Neurons are colour coded by classification, with dashed lines indicating the receptive field thresholds. **h** Preferred direction of female hoverfly OFS DNs after rotating the data 180°. **i** To display all neural data as RHS neurons, we flipped LHS neurons along the midline

(yellow to black). **i** Resulting direction sensitivity after flipping along the midline of the same neuron as in panels b and f. **k** Preferred direction of male hoverfly OFS DNs when displayed as RHS only. **l** Preferred direction of female hoverfly OFS DNs when displayed as RHS only.

Supplementary Fig. 4. Comparison of spontaneous activity and responses to stationary stimuli. a Spontaneous activity (open shapes) and responses of a male OFS DN1 to the stationary starfield (filled shapes), from data extracting directional sensitivity (as in Fig. 2; circles) or velocity response functions (as in Fig. 3; triangles). **b** Spontaneous activity and responses of OFS DN2, displayed as in panel a. **c** WBAS before stimulus presentation (open squares) or when viewing the stationary starfield (filled squares), quantified during velocity response function experiments (as in Fig. 5). **d** Hind leg extension before stimulus presentation (open diamonds) or when viewing the stationary starfield (filled diamonds), quantified during velocity response function experiments (shown in Fig. 7). The data points show data from individual neurons (a and b) or animals (c and d), with lines representing the median. Asterisks denote statistical significance, two-way ANOVA with uncorrected Fisher's LSD test: * $p < 0.05$, ** $p < 0.01$ and *** $p < 0.001$.

Supplementary Fig 5. Morphological quantification of OFS DN2. a Schematic diagram of the hoverfly central brain and thoracic ganglia showing locations where the cervical connective (CC) and the OFS DN2 (orange) widths were measured. **b** Width measurements of OFS DN2 axons along the cervical connective at four anatomical landmarks: (1) immediately posterior to the central brain, (2) upper third of the CC, (3) lower third of the CC, and (4) immediately anterior to the thoracic ganglion. Data are shown for 3 male (blue) and 3 female (red) hoverflies. **c** Width of the anterior end of the cervical connective in the same individuals. All data are presented as individual animals with the horizontal lines indicating median.

Supplementary Fig 6. Impact of stimulus size on neural and behavioural velocity response functions. a Electrophysiological recordings were performed with the hoverfly orientated ventral side up, facing the centre of a horizontally oriented visual display. **b** In behavioural experiments, the hoverfly was tethered at 32º angle, parallel to the ground, facing the centre of a vertically aligned visual display. **c** Velocity response functions of male OFS DN2 neurons when the stimulus covered either the full screen (blue) or the central square (black, N = 7). **d** Velocity response functions of WBAS in male hoverflies when the stimulus covered either the full screen (blue) or the central square (black, N = 5). All data are presented as median and interquartile range.

Supplementary Fig 7. Response onset to sideslip. Onset of head angle, WBAS, fore- and hind legs to sideslip (+2 m/s) in males (N = 6) and females (N = 6). There was no significant difference between body parts, nor males and females (two-way ANOVA, $p = 0.08$, $p = 0.67$ and $p = 0.84$, for body parts, sex and interaction respectively). All data are presented as individual animals with the horizontal lines indicating median.

Supplementary Movies

Supplementary Movie 1. Neural response to roll optic flow. The video shows the raw extracellular response of an OFS DN2 in red when the hoverfly was viewing an example roll stimulus, as in Fig. 3 of the main paper.

Supplementary Movie 2. Female behavioural response to sideslip optic flow. The video on the left shows a female hoverfly filmed from above, with coloured dots indicating the body parts tracked by DeepLabCut to extract wing beat amplitude (WBA), head angle, and fore- and hind leg kinematics. The stimulus viewed by the hoverfly is shown on the right,

with stimulus velocity indicated above the hoverfly video. The movie relates to Fig. 5 of the main paper.

Supplementary Movie 3. Male behavioural response to sideslip optic flow. The video shows a male hoverfly filmed from above, viewing sideslip at different velocities.

Supplementary Movie 4. Female behavioural response to lift. A female hoverfly filmed from above, viewing lift optic flow at different velocities.

Supplementary Movie 5. Male behavioural response to lift. A male hoverfly filmed from above, viewing lift optic flow at different velocities.

Supplementary Movie 6. Female behavioural response to thrust. A female hoverfly filmed from above, viewing thrust optic flow at different velocities.

Supplementary Movie 7. Male behavioural response to thrust. A male hoverfly filmed from above, viewing thrust optic flow at different velocities.

Supplementary Movie 8. Female behavioural response to roll. A female hoverfly filmed from above, viewing roll optic flow at different velocities.

Supplementary Movie 9. Male behavioural response to roll. A male hoverfly filmed from above, viewing roll optic flow at different velocities

Reference cited in Supplementary Information

1 Caliński, T. & Harabasz, J. A dendrite method for cluster analysis. *Communications in Statistics* **3**, 1-27, doi:10.1080/03610927408827101 (1974).

Supplementary Figure 1

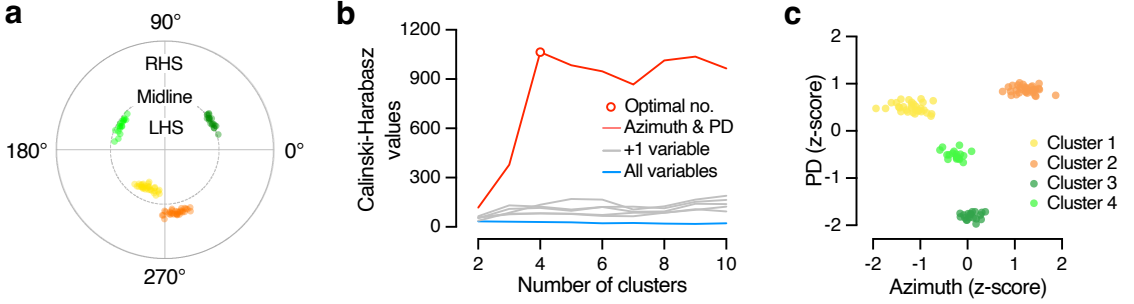

Supplementary Figure 2

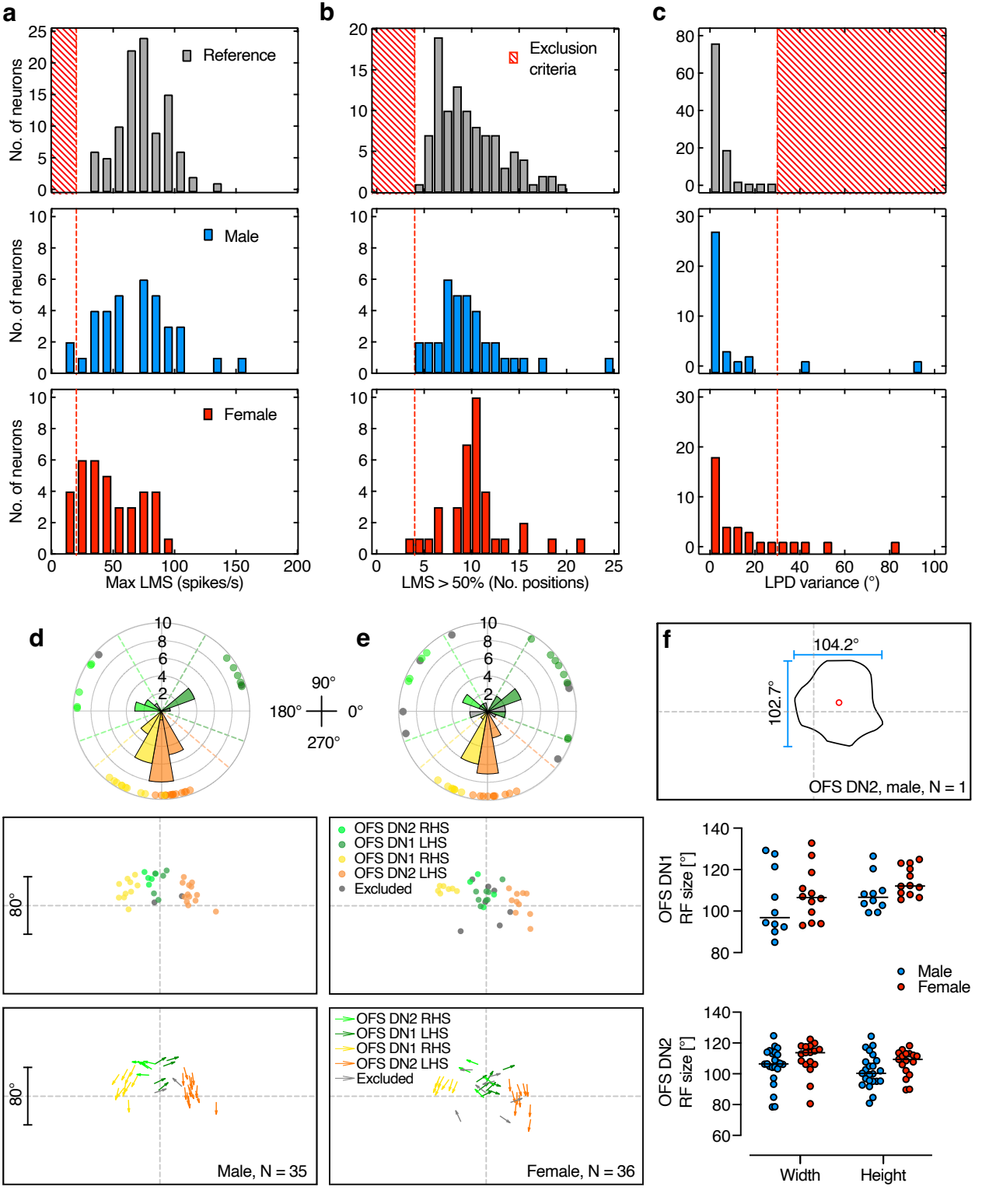

Supplementary Figure 3

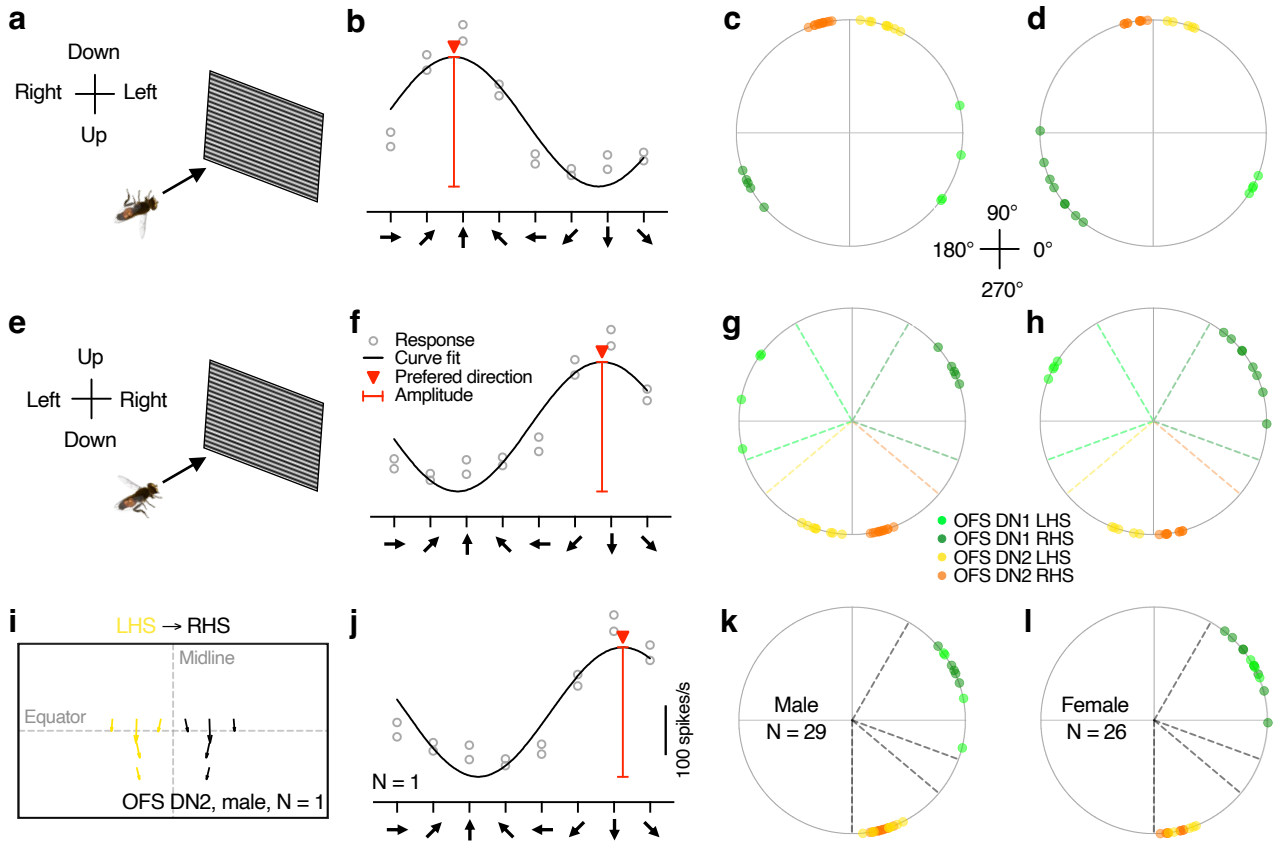

Supplementary Figure 4

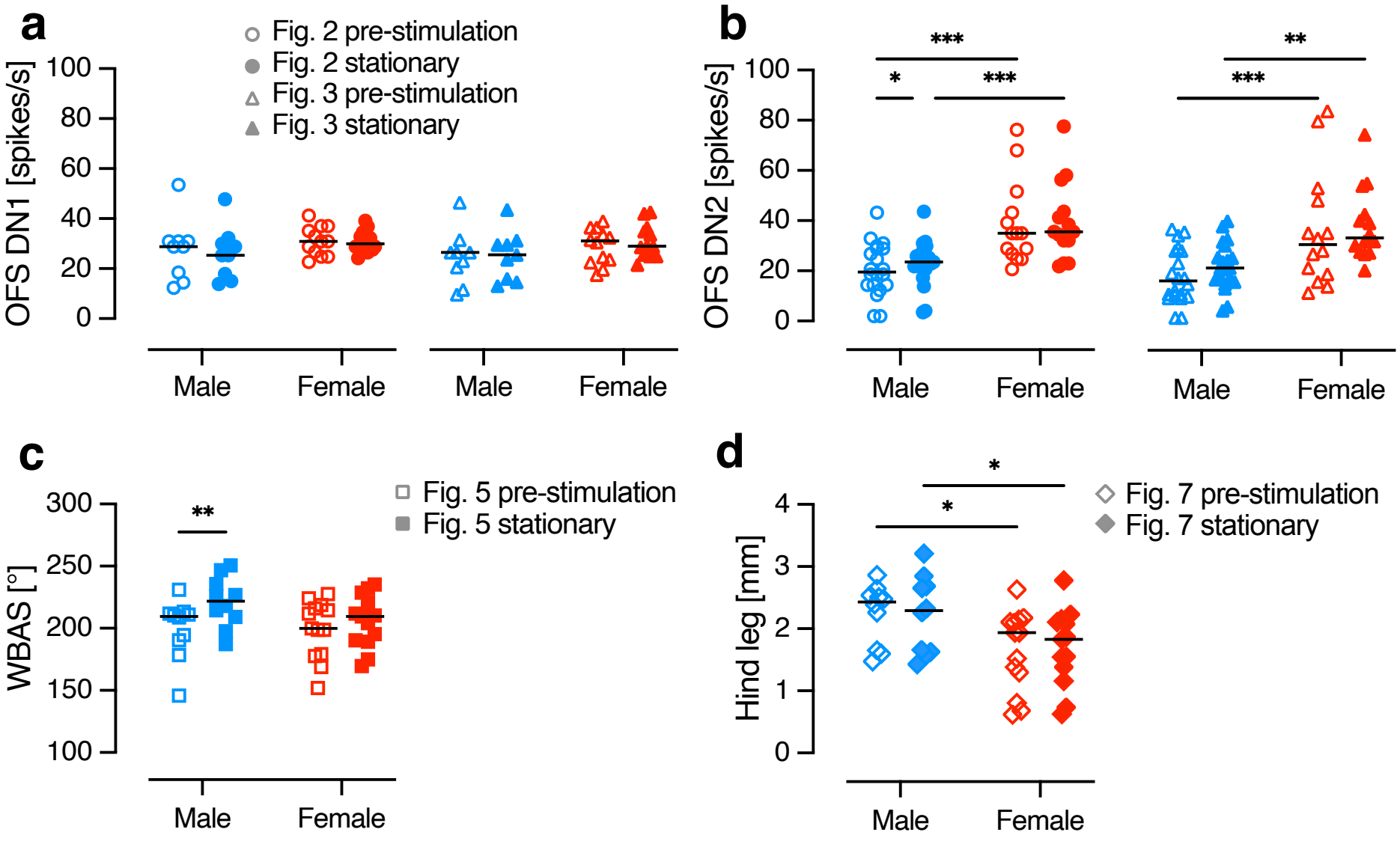

Supplementary Figure 5

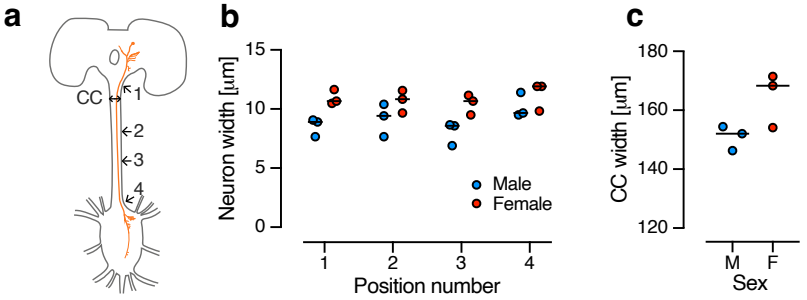

Supplementary Figure 6

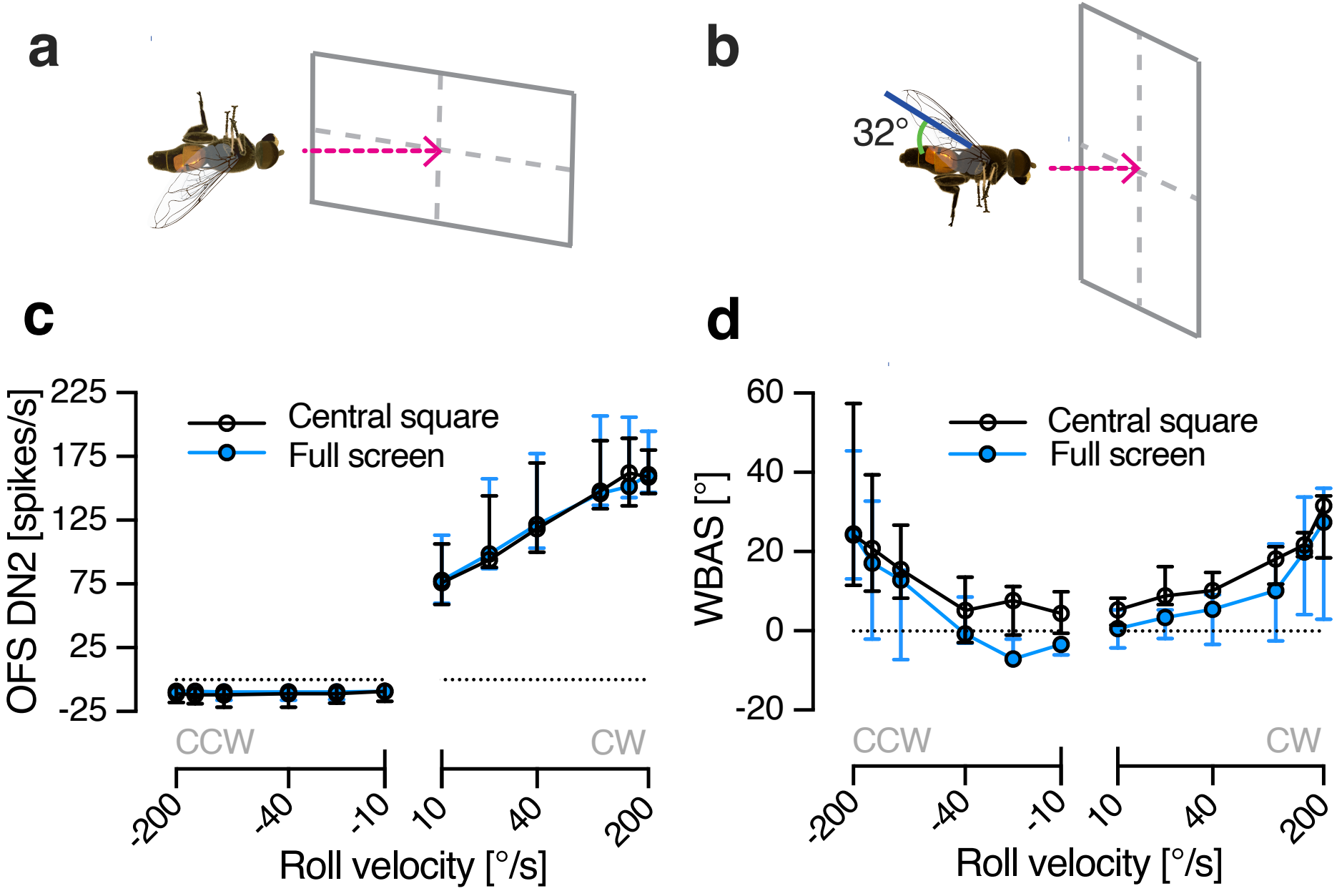
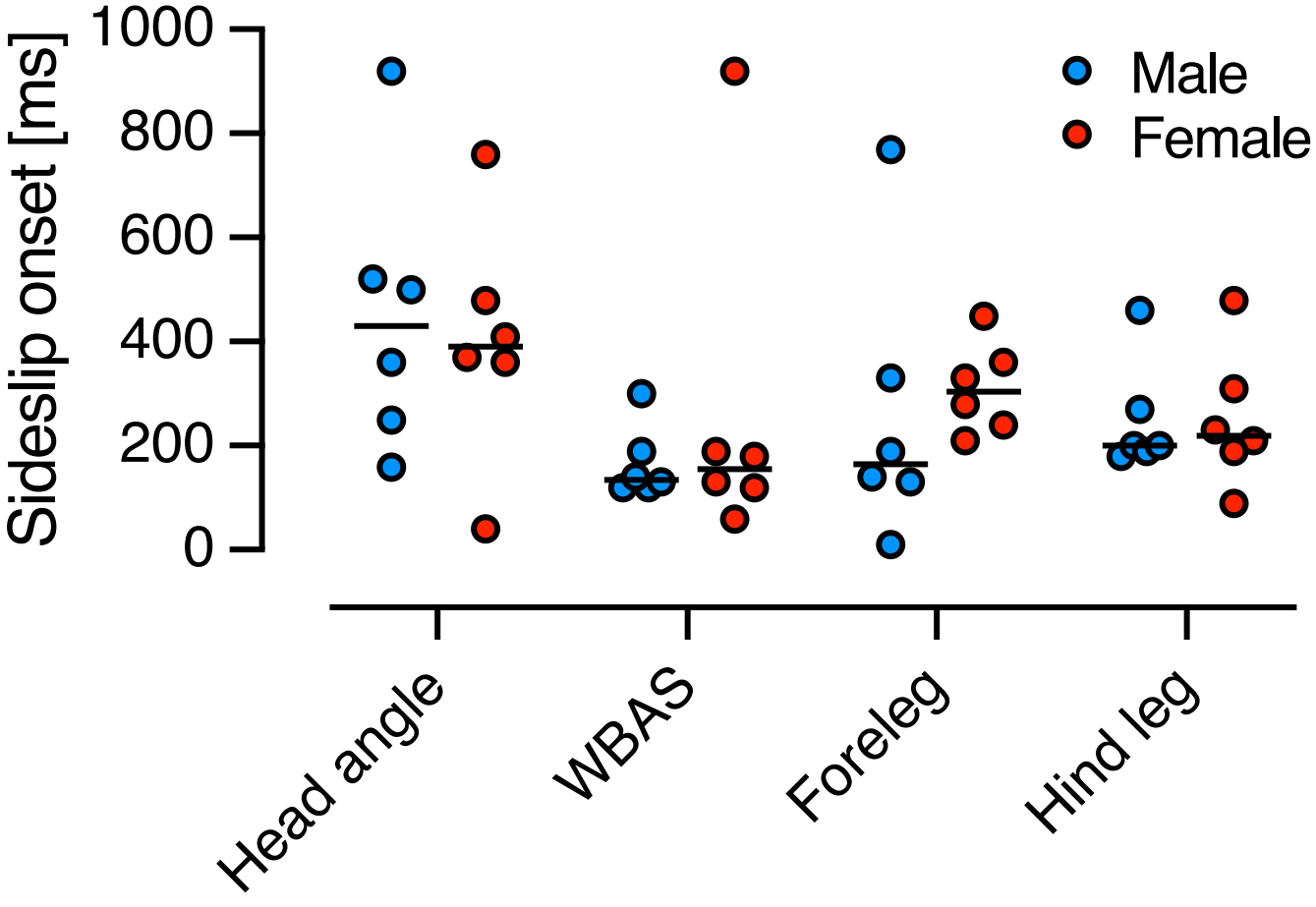
Supplementary Figure 7